DEVELOPMENT OF LIGAND EXCHANGE AND COATING STRATEGIES FOR THE COLLOIDAL QUANTUM DOT BASED HIGH-RESOLUTION SHORT-WAVE INFRARED IMAGING SENSORS

A THESIS SUBMITTED TO
THE GRADUATE SCHOOL OF NATURAL AND APPLIED SCIENCES
OF
MIDDLE EAST TECHNICAL UNIVERSITY

BY

BATUHAN UZUN

IN PARTIAL FULFILLMENT OF THE REQUIREMENTS
FOR
THE DEGREE OF MASTER OF SCIENCE
IN
MICRO AND NANOTECHNOLOGY

JUNE 2024

Approval of the thesis:

DEVELOPMENT OF LIGAND EXCHANGE AND COATING STRATEGIES FOR THE COLLOIDAL QUANTUM DOT BASED HIGH-RESOLUTION SHORT-WAVE INFRARED IMAGING SENSORS

submitted by **BATUHAN UZUN** in partial fulfillment of the requirements for the degree of **Master of Science** i**n Micro and Nanotechnology, Middle East Technical University** by,

Prof. Dr. Naci Emre Altun
Dean, Graduate School of **Natural and Applied Sciences** _____

Prof. Dr. Deniz Üner
Head of the Department, **Micro and Nanotechnology** _____

Assist. Prof. Dr. Demet Asil Alptekin
Supervisor, **Micro and Nanotechnology, METU** _____

Prof. Dr. Tayfun Akın
Co-Supervisor, **Electrical and Electronics Eng., METU** _____

Examining Committee Members:

Prof. Dr. Tayfun Akın
Electrical and Electronics Eng., METU _____

Assist. Prof. Dr. Demet Asil Alptekin
Chemistry, METU _____

Assoc. Prof. Dr. Kıvanç Azgın
Mechanical Eng., METU _____

Assoc. Prof. Dr. Hasan Tarık Baytekin
Chemistry, METU _____

Assist. Prof. Dr. Emre Ozan Polat
Physics, Bilkent University _____

Date: 13.06.2024

I hereby declare that all information in this document has been obtained and presented in accordance with academic rules and ethical conduct. I also declare that, as required by these rules and conduct, I have fully cited and referenced all material and results that are not original to this work.

Name Last name : Batuhan Uzun

Signature :

ABSTRACT

DEVELOPMENT OF LIGAND EXCHANGE AND COATING STRATEGIES FOR THE COLLOIDAL QUANTUM DOT BASED HIGH-RESOLUTION SHORT-WAVE INFRARED IMAGING SENSORS

Uzun, Batuhan
Master of Science, Micro and Nanotechnology
Supervisor: Assist. Prof. Dr. Demet Asil Alptekin
Co-Supervisor: Prof. Dr. Tayfun Akın

June 2024, 85 pages

InGaAs is still in use due to its high sensitivity for Short-Wave Infrared (SWIR) imaging sensor technology. However, InGaAs has disadvantages such as high production and raw material costs and long production conditions, as well as the problems encountered during the hybridization process. Limited resources are also an obstacle to the development of areas such as the automotive and defense industries where such sensors are needed. In this respect, sensors based on PbS colloidal quantum dots are considered the best material candidates as an alternative to InGaAs. PbS colloidal quantum dots can be easily produced monolithically on a chip at a low cost. However, the PbS quantum dot layer needs to go through many post-synthesis steps. Yet, the recently introduced direct synthesis method allows one-step PbS CQD ink synthesis which eliminates complex ligand exchange steps. Despite its infantile stage, with slight optimizations, the photodiodes that reached 10^{13} Jones detectivities in the IR region were produced in this thesis. Moreover, the low dark current density around 10^{-8} mA.cm^{-2} and fast rise/fall time (1.65/8.08 μs) were achieved. In addition to these promising photodetector performance parameters achieved by increasing the

quantum dot quality, production costs were also reduced with the optimization studies at the synthesis stage. In this context, the production yield of QDs increased by 42%. Furthermore, a detailed SCAPS study was conducted, and the optimal device architecture was identified. Moreover, a numerical comparison between p-type and n-type inks revealed that the p-type ink could lead to a better device performance.

Keywords: Colloidal Quantum Dot, Ligand Exchange, Photodetector, Short-Wave Infrared Imaging Sensor

ÖZ

KOLOİDAL KUANTUM NOKTA TABANLI YÜKSEK ÇÖZÜNÜRLÜKLÜ KISA DALGA KIZILÖTESİ GÖRÜNTÜLEME SENSÖRLERİ İÇİN LİGAND DEĞİŞİMİ VE KAPLAMA STRATEJİLERİNİN GELİŞTİRİLMESİ

Uzun,Batuhan
Yüksek Lisans, Mikro ve Nanoteknoloji
Tez Yöneticisi: Dr. Öğr. Üyesi Demet Asil Alptekin
Ortak Tez Yöneticisi: Prof. Dr. Tayfun Akın

Haziran 2024, 85 sayfa

InGaAs, Kısa Dalga Kızılötesi (SWIR) görüntüleme sensörü teknolojisinde yüksek hassasiyeti nedeniyle halen kullanılmaktadır. Ancak InGaAs yüksek üretim ve hammadde maliyetleri ve uzun üretim koşulları gibi dezavantajlarının yanı sıra hibridizasyon sürecinde karşılaşılan problemlere sahiptir. Sınırlı kaynaklar bu sensörlerin ihtiyaç duyulduğu otomotiv ve savunma gibi sekörlerdeki gelişimine engel teşkil etmektedir. Bu açıdan, PbS koloidal kuantum noktalarına dayalı sensörler, InGaAs teknolojisine alternatif olarak en iyi malzeme adayları olarak kabul edilmektedir. PbS koloidal kuantum noktaları, düşük bir maliyetle bir çip üzerinde monolitik olarak kolayca üretilebilir. Ancak PbS kuantum nokta katmanının birçok sentez sonrası aşamadan geçmesi gerekiyor. Yeni tanıtılan doğrudan sentez yöntemi, kompleks ligand değişim adımlarını ortadan kaldırarak tek adımda PbS CQD mürekkep sentezine imkan tanır. Gelişme aşamasında olmasına rağmen, bu tezde yapılan optimizasyonlarla, kızıl-ötesi alanda 10^{13} Jones mertebelerine ulaşan fotodiyotlar üretilmiştir. Ayrıca 10^{-8} mA.cm^{-2} civarında düşük karanlık akım yoğunluğu ve hızlı yükselme/düşme süresi (1.65/8.08 µs) elde edildi.

Kuantum nokta kalitesinin artırılmasıyla elde edilen bu umut verici fotodedektör performans parametrelerinin yanı sıra sentez aşamasında yapılan optimizasyon çalışmaları ile üretim maliyetleri de düşürüldü. Bu kapsamda QD'lerin üretim verimi %42 oranında artırıldı. Ayrıca detaylı bir SCAPS çalışması yapılarak en uygun cihaz mimarisi belirlendi. Ayrıca, p tipi ve n tipi mürekkepler arasında yapılan sayısal bir karşılaştırma, p tipi mürekkebin daha iyi bir cihaz performansı sağlayabileceğini ortaya çıkardı.

Anahtar Kelimeler: Kolloidal Kuantum Nokta, Ligand Değişimi, Fotodedektör, Kısa Dalga Kızılötesi Görüntüleme Sensörü

To my beloved family…

ACKNOWLEDGMENTS

Words cannot express my gratitude to my lovely family, my parents Pınar Uzun and İhsan Uzun and my brother Teoman Uzun for their support throughout my life.

I could not have undertaken this journey without Assist. Prof. Dr. Demet Asil Alptekin. I would like to express my deepest appreciation for her sincere and hard efforts.

I would like to thank my co-advisor Prof. Dr. Tayfun Akın for his interest in this study.

Also, I am extremely grateful to Firdevs Aydın for her help during synthesis and characterization steps and İrem Kolay for her guidance.

I would like to thank Emrah Dirican for our theoretical discussions that helped me gain a deeper understanding of the subject and for his support throughout the study.

I express my profound gratitude to the METU MEMS Center for their invaluable contributions that have enabled the realization of this study.

I am also grateful to Scientific and Technological Research Council of Turkey (TÜBİTAK) for the financial support (Project Code: 123M739).

Finally, I would like to thank Sevcan Erel for always being there for me whenever I struggled, and for consistently being understanding and motivating throughout my journey.

TABLE OF CONTENTS

ABSTRACT v

ÖZ vii

ACKNOWLEDGMENTS x

TABLE OF CONTENTS xi

LIST OF TABLES xiv

LIST OF FIGURES xv

LIST OF ABBREVIATIONS xviii

CHAPTERS

1 INTRODUCTION 1

2 BACKGROUND 3

2.1 Colloidal Quantum Dots 3

2.2 Synthesis of Nanoparticles via Hot Injection Method 5

2.3 Synthesis of PbS Colloidal Quantum Dots via Hot Injection Method 7

2.4 Ligand Exchange Mechanisms for PbS CQDs and PbS Ink Preparation Methods 8

2.4.1 Solid State Ligand Exchange of PbS CQDs 11

2.4.2 Phase Transfer Ligand Exchange and PbS Ink 11

2.4.3 Direct Synthesis of PbS Ink 12

2.5 Photodiodes 13

2.5.1 Working Principle of PIN Photodiodes 14

2.5.2 Figures of Merit for Photodiodes 16

2.5.2.1 Dark Current 16

2.5.2.2 External Quantum Efficiency 17
2.5.2.3 Noise Equivalent Power 17
2.5.2.4 Specific Detectivity 18
2.5.2.5 Response Time 18
2.6 PbS CQD Photodiodes for SWIR Detection 19
2.7 Device Architecture of PbS CQD Photodiodes 20
2.8 SCAPS 1-D Simulation 24
3 EXPERIMENTAL 25
3.1 Materials 25
3.2 Synthesis and Ink Preparation 25
3.2.1 ZnO NP Synthesis via Hot Injection Method 26
3.2.2 PbS CQD Synthesis via Hot Injection Method and PbS CQD Ink Preparation by PTLE Approach 26
3.2.3 Direct Synthesis of PbS CQD Ink 28
3.3 Material Characterization / Instrumentation 29
3.3.1 Absorption Spectroscopy 29
3.3.2 Transmission Electron Microscopy 29
3.3.3 Fourier-transform Infrared Spectroscopy 30
3.3.4 Scanning Electron Microscopy 30
3.3.5 Photoluminescence 30
3.4 Photodiode Simulation 30
3.5 Photodiode Fabrication 32
3.6 Photodiode Characterization 34
3.6.1 Wire Bonding 34

3.6.2 Current Voltage Measurement 36
3.6.3 External Quantum Efficiency Measurement 36
3.6.4 Rise Time & Fall Time Measurement 37
3.6.5 Capacitance-Voltage (C-V) Measurement 39
4 RESULTS AND DISCUSSION 41
4.1 Characterization of the PTLE and DS PbS CQD Inks 41
4.2 SCAPS Simulation Results for the Device Architecture 44
4.3 Comparison of PTLE & DS PbS Ink Devices 46
4.3.1 Current-Voltage Measurement Results 46
4.3.2 EQE, Spectral Response and Specific Detectivity Results 48
4.3.3 Rise & Fall Time Measurement Results 49
4.3.4 Overall Comparison 52
4.4 Further Optimization of DS PbS CQD Based Photodiodes 53
4.5 The Future Potential of DS PbS Ink Through SCAPS 61
4.5.1 ETL and HTL Combination Study 65
4.5.2 The Effect of Dopant Type 67
4.6 Output of the Study 71
5 CONCLUSION AND FUTURE PROSPECT 73
REFERENCES 77

LIST OF TABLES

TABLES

Table 2.1. Summary of the photodetector performance parameters of the state of art PbS CQD based photodiodes.....22
Table 3.1. The basic SCAPS parameters for ZnO, PbS Ink and PbS-EDT layers. .31
Table 4.1 Comparison of the photodiodes that are produced within this study. 53
Table 4.2. The basic SCAPS parameters for DS PbS Ink and HTLs. 63
Table 4.3. The basic SCAPS parameters for DS PbS Ink and HTLs. 64
Table 4.4. Comparison of the simulated and reported ITO/ZnO/DS PbS ink/PbS-EDT/Au cell.....65

LIST OF FIGURES

FIGURES

Figure 2.1. Schematic representation of relation between bandgap energy (E_G) and size of quantum dots. 4
Figure 2.2. **a)** Depiction of a customary configuration employed in the hot injection technique. **b)** Illustration of the nucleation and growth mechanisms in accordance with the LaMer-Dinegar model..... 6
Figure 2.3. The progress of infrared colloidal quantum dot solar cells in terms of power conversion efficiency (PCE) from 2009 to 2019 (validated by NREL).[19]..... 9
Figure 2.4. **a)** Representation of solid-state ligand exchange (L-B-L) and solution phase ligand exchange (PTLE). **b)** Representation of the direct synthesis PbS inkstrategy (DS-PbS ink).[23] 10
Figure 2.5. **a)** Cross section of a p-n photodiode **b)** Cross section of a PIN photodiode..... 15
Figure 2.6. The band diagram of P-I-N photodiode under zero bias. 16
Figure 2.7. **a)** Device architecture of a PbS CQD based photodiode and **b)** working principle of photodiode based on its energy bandgap in eV. 21
Figure 3.1. **a)** Before injection. **b)** After injection. 27
Figure 3.2. Schematic of the photodiode fabrication process. 32
Figure 3.3. L-B-L technique for PbS-EDT layer. 33
Figure 3.4. **a)** Top side of produced photodiode. **b)** Bottom side of produced photodiode..... 33
Figure 3.5. F&K Delvotec Wedge 5630 wire bonding system. 34
Figure 3.6. **a)** Photodiode after wire bonding. **b)** Photodiode after getting contact cable. **c)** Bottom side of photodiode. **d)** Top side (illuminated side) of photodiode. 35
Figure 3.7. **a)** Keithley 2425 device, **b)** connection of the photodiode to the Keithley 2425. 36

Figure 3.8. **a)** Newport QUANTX-300 external quantum efficiency measurement setup. **b)** On going measurement on a PbS CQD photodiode integrated into PCB.37
Figure 3.9. **a)** Agilent MSO-X4034A Mixed Signal Oscilloscope. **b)** Agilent 3322A 20 MHz function / arbitrary waveform generator. **c)** The connection of a sample to the oscilloscope. **d)** Validating the signal via green LED. **e)** Shining green LED onto the sample to control the parameters. **f)** TSAL6200 GaAlAs 940nm high-power infrared LED. 38
Figure 3.10. C-V measurement setup. 39
Figure 4.1. **a)** Absorbance of 1.3 eV PbS-OA CQD. **b)** TEM image of PbS CQD.41
Figure 4.2. Absorbance of the thin film PbS-OA, EDT ligand exchanged (L-B-L) PbS CQD, PbS CQD ink derived from PTLE method and PbS CQD ink synthesized via DS method. 42
Figure 4.3. FTIR spectra of PbS-OA, PTLE PbS CQD ink, and DS PbS CQD ink. 43
Figure 4.4. Device structure of PbS CQD photodiode for SCAPS **a)** top illuminated **b)** bottom illuminated. 44
Figure 4.5. SCAPS **a)** I-V and **b)** EQE performance of PbS CQD photodiode for top and bottom illuminations. 45
Figure 4.6. I-V results for photodiode devices with **a)** DS PbS Ink and **b)** PTLE PbS Ink. 47
Figure 4.7. **a)** EQE, **b)** spectral response, and **c)** specific detectivity results for both device with DS PbS Ink and PTLE PbS Ink. 48
Figure 4.8. **a)** The rise/fall time signals in a larger scale, **b)** closer look to the rise time, **c)** closer look to the fall time signals for devices with DS PbS Ink. 50
Figure 4.9. **a)** The rise/fall time signals in a larger scale, **b)** closer look to the rise time, **c)** closer look to the fall time signals for devices with PTLE PbS Ink. 51
Figure 4.10. **a)** Experimental notations for this study. **b)** Representation of the pixel orders. 52
Figure 4.11. Representation of **a)** Reaction-1 and **b)** Reaction-2. 54
Figure 4.12. Normalized PL intensity comparison for **a)** R1 ink and **b)** R2 ink. 54

Figure 4.13. **a)** Absorption spectrum of R1 and **b)** absorption spectrum of R2 at different reaction times. 55
Figure 4.14. **a)** Band edge absorption as a function of time for R1 and R2.**b)** Change of FWHM with time for R1 and R2..... 56
Figure 4.15. R1 and R2 device comparison in terms of **a)** dark current, **b)** EQE, **c)** spectral response, **d)** specific detectivity in ITO/ZnO/DS PbS Ink/PbS-EDT/Au architecture. Cross sectional SEM image of **e)** R1 device, **f)** R2 device. 57
Figure 4.16. Response time of R1 where **a)** large scale, **b)** rise time, **c)** fall time and response time of R2 where **d)** large scale, **e)** rise time and **f)** fall time. 59
Figure 4.17. Capacitance-Voltage measurements and Mott-Schottky analysis for **a)** device with R1 and **b)** device with R2. **c)** calculated depletion width of ITO/ZnO/DS PbS Ink R1 or R2/ PbS-EDT/Au device..... 60
Figure 4.18. ETL (thickness = 100 nm) and HTL (thickness = 50 nm) combinations for DS PbS ink (thickness = 300 nm) based solar cells where the ETLs are: **(a)** ZnO, **(b)** TiO_2, **(c)** IGZO, **(d)** SnO_2, **(e)** C_{60}, **(f)** CdS, **(g)** CeO_2. 66
Figure 4.19. Concurrent effect of donor concentration and acceptor concentration vs. defect density on Voc (**a**,**b**), Jsc (**c**,**d**), FF (**e**,**f**), and PCE (**g**,**h**) parameters for the champion cell structure. The thickness of DS PbS ink was fixed at 300nm..... 68
Figure 4.20. Electrical field intensity distribution in the ITO/TiO_2/ p-type DS PbS ink/ MoO_3/Au device architecture where the defect density was set at 10^{13} cm^{-3}.. 70

LIST OF ABBREVIATIONS

ABBREVIATIONS

CQDs : Colloidal Quantum Dots

PbS : Lead Sulfide

SWIR : Short-Wave Infrared

InGaAs: Indium Gallium Arsenide

ROIC : Readout Integrated Circuit

E_G(QD): Bandgap Energy of Quantum Dot

E_{Bulk} : Energy of a Bulk Semiconductor

PTLE : Phase Transfer Ligand Exchange

NPs : Nanoparticles

NC : Nanocrystal

PbO : Lead Oxide

OA : Oleic Acid

ODE : Octadecene

$(TMS)_2S$: Bis-trimethylsilyl sulfide

L-B-L : Layer by layer

OAm : Oleylamine

SSLE : Solid-State Ligand Exchange

SPLE : Solution Phase Ligand Exchange

PCE : Power Conversion Efficiency

I_2 : Iodine

Br : Bromide

DS : Direct Synthesis

DPhTA: Diphenylthiourea

BTA : Butylamine

TBAI : Tetrabutylammonium Iodide

EMII : 1-Ethyl-3-Methylimidazolium Iodide

MPA : 3-Mercaptopropionic Acid

ACN : Acetonitrile

MeOH : Methanol

DMF : Dimethylformamide

I_{dark} : Dark Current

EQE : External Quantum Efficiency

NEP : Noise Equivalent Power

D* : Specific Detectivity

$I_{saturation}$: Saturation Current

V_{oc} : Open Circuit Voltage

J_{sc} : Short Circuit Current Density

FF : Fill Factor

PL : Photoluminescence

EDT : Ethane-1,2-dithiol

ZnO : Zinc Oxide

MoO_3 : Molybdenum Trioxide

TiO_2 : Titanium Dioxide

HTL : Hole Transport Layer

ETL : Electron Transport Layer

C-V : Capacitance – Voltage

SEM : Scanning Electron Microscopy

TEM : Transmission Electron Microscopy

SCAPS: Solar Cell Capacitance Simulator

FWHM: Full Width at Half Maximum

J_D : Dark Current Density

CHAPTER 1

INTRODUCTION

Colloidal Quantum Dots (CQDs) are very popular among many photonic applications, such as solar cells, write th elong name (LEDs), and especially imaging systems, as they have adjustable band gap and easy processing steps which makes them also suitable for many industries like defence, automobile, and energy. For Short-Wave Infrared (SWIR) imaging systems, lead sulfide (PbS) CQDs are considered very prominent candidates not only because of their optoelectronic properties but also their state-of-the-art figures of merit[1]. The high production and raw material costs of conventional indium gallium arsenide (InGaAs) based SWIR imaging sensors make PbS CQD based SWIR imaging sensors more feasible in economical aspect. In addition to that, flip-chip bonding technique is widely used in the production of today's hybrid InGaAs based devices.[2] Flip-chip bonding technique is basically based on connecting each pixel with indium to the silicon readout integrated circuit (ROIC). Silicon-based ROIC is connected to the detector in a process called "hybridization".[2] In this way, electron (e^-) - hole (h^+) pairing can be created by absorbing infrared radiation, then transmitting the signal to the ROIC via metal electrodes and indium. Among the main reasons why indium is preferred in the hybridization process are its good bonding feature with commonly used detector materials, and its flexibility even at low temperatures. However, the mismatch in the thermal expansion coefficients of the silicon and detector materials causes stress on the indium bonds, and due to this situation, the indium bonds are broken[2]. PbS CQDs, on the other hand, can be processed directly from the solution and can therefore be easily integrated.[1,3]

This study aims to show the real potential of PbS CQD structures in the photodetector field by developing new strategies for the ligand exchange, coating steps, keeping the trap bands under control, and increasing their stability under atmospheric conditions.

In Chapter 2, necessary background information and theoretical information are given to understand and interpret the study. Firstly, basic information about CQDs is provided. Secondly, the widely used hot injection synthesis method and Layer-by Layer (LBL) ligand exchange strategy are explained. Then, another widely used ligand exchange strategy, called phase transfer ligand exchange (PTLE) method is explained. Finally, recently reported direct synthesized (DS) PbS ink strategy is discussed and the working principles and architecture of the photodiodes are shared.

In Chapter 3, the experimental procedures that are followed during this study are given in detail. Synthesis, purification methods and characterization techniques are shared.

In Chapter 4, the characterizations of the PTLE and DS PbS ink are shared. Followingly, the device architecture through numerical analysis was investigated. It had been seen that ITO/ZnO/PbS ink/PbS-EDT/Au structure was more efficient than ITO/PbS-EDT/PbS ink/ZnO/Au. After setting up the device architecture, DS and PTLE inks were compared and DS PbS inks were found to have higher specific detectivity values. Following this, an optimization study on the DS PbS ink synthesis was carried out which improved the rate of reaction and enhanced the specific detectivity (up to 10^{13} Jones) and decreased rise/fall time to 1.65/8.08 μs. Finally, systematic simulations had been conducted to reveal the true potential of DS PbS ink where the best device architecture was found for this ink as ITO/TiO_2/DS PbS ink/ MoO_3/Au and the effect of doping type of DS PbS ink was elaborated. It was concluded that the p-type ink could lead to higher performance for these photodiodes compared to the n-type ink.

CHAPTER 2

BACKGROUND

2.1 Colloidal Quantum Dots

Colloidal Quantum Dots (CQDs) are semiconductor materials that display 3-dimensional quantum confinement effect, and they are also known as nanocrystals or artificial atoms. In recent years, there has been a lot of interest in these materials due to their high spectral tunability via synthesis stages and unique physical, chemical, and optoelectronic properties.[4] Due to those properties, these materials play important roles in different device fabrications such as solar cells, photodetectors, imaging sensors, and light emitting diodes. One of the most important features of CQDs is the ability of easy bandgap tunability through the size of particles.[4] This bandgap tunability feature enables the determination and optimization of absorption profile for the infrared photodetectors and imaging sensors to match the infrared portion of electromagnetic spectrum. Especially the infrared active PbS CQDs are widely considered for the infrared photodetectors due to their high absorption coefficient, large Bohr radius, narrow bulk band gaps, and high quantum confinement effect.[5]

Brus (1984) proposed the first theoretical calculation to find the energy bandgap of a spherical quantum dots based on effective mass approximation:

$$E_g(QD) = E_{Bulk} + \frac{h^2}{8R^2}\left(\frac{1}{m_e^*} + \frac{1}{m_h^*}\right) - \frac{1.8e^2}{4\pi\varepsilon_0\varepsilon_r R^2}$$

where $\mathbf{E_G(QD)}$ represents the bandgap energy of the quantum dot, $\mathbf{E_{Bulk}}$ is the energy of a bulk semiconductor, **h** is the Planck's constant, **R** is the radius of quantum dot, $\boldsymbol{m_e^*}$ is the effective mass of excited electron, $\boldsymbol{m_h^*}$ is the effective mass of excited hole,

$\boldsymbol{\varepsilon_0}$ is the permittivity of vacuum, and $\boldsymbol{\varepsilon_r}$ is the relative permittivity.[6] This formulation earned Louis Edward Brus the Nobel Prize in 2023 for his contributions to chemistry. As the Brus equation states, a spherical shaped quantum dot's energy bandgap is inversely proportional to the square of the radius of quantum dot and this relation can be seen in Figure 2.1.

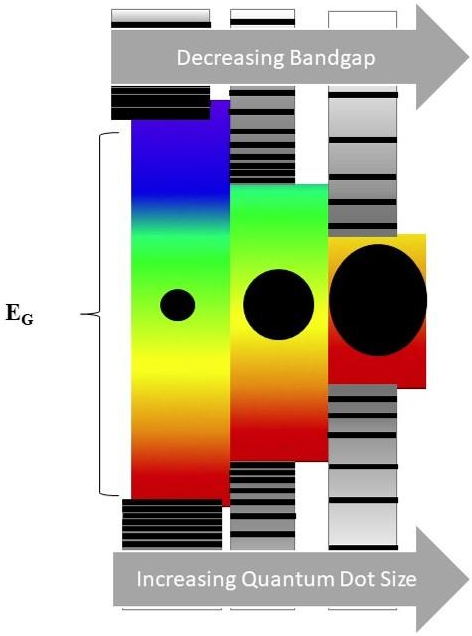

Figure 2.1. Schematic representation of relation between bandgap energy (E_G) and size of quantum dots.

The increased bandgap energy means higher confinement energy for a quantum dot.[7] Higher quantum confinement energy is responsible for the collapse of continuous energy band spectrum into the discrete energy levels within the bulk materials. This discrete structure causes discrete absorption spectrum for CQDs whereas bulk semiconductors have continuous absorption spectrum.

2.2 Synthesis of Nanoparticles via Hot Injection Method

It is crucial to carefully select the best synthesis method and carefully manage reaction conditions in order to produce nanoparticles. For the production of PbX quantum dots (where X stands for Se, S, or Te), the hot injection synthesis method is frequently used. It stands out for its affordability, simplicity of preparation, and high manufacturing yield. Rapid nucleation is followed by continuous growth stages in this approach.[8] It is possible to create crystals of different sizes and morphologies by adjusting the reaction parameters, such as the precursors' reactivity and concentration, the temperature during the injection and growth stages, as well as the length of the growth process.[9] The theoretical framework developed by LaMer and Dinegar is significantly used in current methods for producing uniform nanoparticles. This model proposes a discrete temporal sequence of events, commencing with nucleation, followed by regulated and slow development on the existing nuclei, to generate monodisperse nanoparticles.[10,11] An exemplary process of synthesizing nanoparticles, as depicted schematically in Figure 2.2-a, commences by introducing appropriate molecular precursors into a reaction mixture, thus yielding "monomers" that facilitate the homogeneous formation of NPs. Subsequently, the growth of NPs ensues owing to the continuous influx of monomers onto the surface of the NPs. Figure 2.2-b illustrates that the diminishing concentration of monomers initiates the phenomenon known as Ostwald ripening, also referred to as Lifshitz–Slyozov–Wagner growth, wherein smaller dots dissolve while larger ones emerge.[12,13]

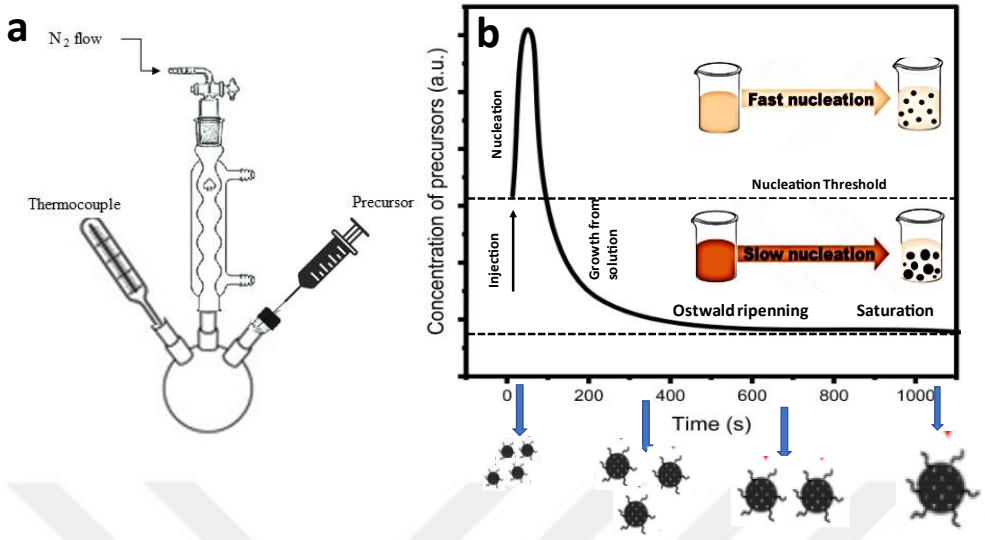

Figure 2.2. **a)** Depiction of a customary configuration employed in the hot injection technique. **b)** Illustration of the nucleation and growth mechanisms in accordance with the LaMer-Dinegar model.

The creation of bigger dots with a lower band gap as a result of this process may result in a red shift in the absorbance spectra. Additionally, by adversely influencing the size distribution, it has the potential to impair the quality of the nanoparticles (NPs).[12] It is crucial to exert control over the length of growth in order to avoid the Ostwald ripening process from occurring. The presence of capping ligands, also referred to as stabilizers or surfactants, is crucial during the nanoparticle and colloidal quantum dot (CQD) synthesis. These molecules, including long chain carboxylic acids, phosphonic acids, alkyl thiols, alkyl phosphines, alkyl phosphine oxides, and alkylamines, attach to the surface of the CQDs and regulate the kinetics of nucleation and growth, while also imparting both colloidal and chemical stability. Moreover, the initial concentration of the stabilizers exerts a significant influence on both the quality and monodispersity of the NPs.[14] The concentration of capping ligands has an effect on the speed of nucleation and the resulting size distribution of CQDs. As shown in Figure 2.2-b, a high concentration of capping ligands leads to slow nucleation and a wide size distribution, whereas a diluted concentration results

in fast nucleation and the formation of CQDs with a homogeneously distributed size.[15] As a result, the technique known as the "hot injection method" involves quickly injecting one precursor into another within a heated solvent, which causes monomers to form as soon as possible by fast nucleation. Non-coordinating and chemically inert liquids with high boiling points are often preferred to widen the reaction's temperature range. The growth time, injection temperature, growth method, and precursor concentration, in addition to the injection rate and the concentration of the capping ligand, have an influence on the size and size distribution of the CQDs or NPs.

2.3 Synthesis of PbS Colloidal Quantum Dots via Hot Injection Method

The synthesis of PbS CQDs is possible with hot injection method and employs a Schlenk line system that incorporates a two-way flow mechanism. One side of the system exposes the synthesis environment to an inert gas, typically nitrogen, which does not participate in the reaction, while the other side allows for the system to be evacuated by vacuum. With the adjustable valves in the Schlenk line, the system can be switched between nitrogen or vacuum conditions as required. In the synthesis of PbS quantum dots, lead oxide (PbO) precursor is mixed and dissolved in a solution of oleic acid (OA) and octadecene (ODE). Subsequently, the mixture is transferred to a three-neck reaction flask connected to the Schlenk line, and a magnetic stir bar should be added. The mixture can be stirred under vacuum until it reaches the desired temperature. During this process, the lead oxide in the reaction flask completely dissolves, forming Pb (lead) - OA complexes.[16] The resulting complex solution changes color from yellow to transparent. The reaction temperature is initially set to the coordination temperature and then adjusted to the injection temperature. As a sulfur precursor, bis-trimethylsilyl sulfide $(TMS)_2S$ is dissolved in ODE and mixed together.[16,17] This prepared solution should be rapidly injected into the reaction flask. It is crucial to perform the injection rapidly in order to obtain a product with a monodisperse distribution.[16,17] After the injection, the solution is expected to change

color from transparent to cloudy black. Following the desired growth time of the quantum dots, the reaction flask is cooled to terminate the growth stage. Following the synthesis, the synthesized PbS CQDs can be subjected to purification steps to remove impurities and unwanted byproducts. After purification, oleate capped PbS CQDs can be redispersed in a nonpolar solvent for further characterization or applications.[17]

The long alkyl chains (oleate ligands) present on the surfaces of PbS quantum dots provide them with colloidal properties but hinder electrical conductivity. Therefore, it is necessary to replace these ligands during electronic device applications. The reason is that the presence of long ligand chains is blocking the transportation of the charge carriers. To prevent and maintain the electronic conductivity in a device, these long-chain ligands should be replaced by short ones for the PbS CQD films.[18] The method and choice of ligand for ligand exchange are crucial factors that can significantly impact the performance characteristics and lifespan of the final electronic device.[18]

2.4 Ligand Exchange Mechanisms for PbS CQDs and PbS Ink Preparation Methods

As mentioned in the previous section, the synthesis of PbS CQD was typically carried out through wet chemistry organometallic methods, wherein long-chain organic ligands like OA or oleylamine (OAm) are used to cover the surface of the dots. This serves to stabilize the colloidal system in the solvent. Yet, it is essential to remove these long-chain ligands to shorter ones for many electronic applications since the long-chain ligands are acting as insulators. There are two main ways to change these long-chain ligands with shorter ones: solid-state ligand exchange (SSLE) and solution phase ligand exchange (SPLE) or also known as phase transfer ligand exchange (PTLE).[19] SSLE is accepted as more conventional way to produce PbS CQD films where the layer by layer (L-B-L) approach is mainly preferred for the deposition of PbS CQDs.[19] However, the unavoidable considerable volume

shrinkage produced by this traditional approach would result in unwanted cracks and irregular QD distribution in the film, in addition to increased densities of defects and an inhomogeneous energy landscape.[20] On the other hand, PTLE method is more promising way to produce PbS CQDs in the recent years as seen in Figure 2.3. The reason is that PTLE method is allowing to produce more uniform, less rough and pinhole-free PbS CQD films as compared to SPLE.[21] Moreover, the PTLE method facilitates the exchange of ligands within the solution, resulting in the acquisition of concentrated colloidal quantum dot (CQD) ink where short ligands cap the surface of the PbS CQDs.[19] At the end, PbS CQDs are surrounded by iodine (I_2) (known as PbS ink) can be directly coated onto substrates in a single step as seen in Figure 2.4-a. This opens up the way for the production of industrially viable and more optimized PbS quantum dot-based photodiodes.

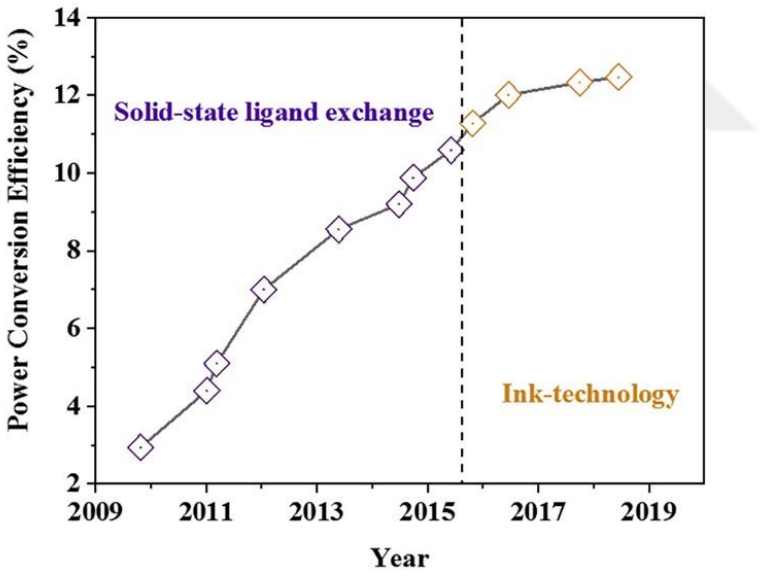

Figure 2.3. The progress of infrared colloidal quantum dot solar cells in terms of power conversion efficiency (PCE) from 2009 to 2019 (validated by NREL).[19]

Apart from these two techniques, it is possible to obtain PbS CQD ink from a method known as direct synthesis (DS).[19] This approach is more readily scalable, which supports the potential for future large-scale production of printable devices.[22] In

addition to that, DS method achieved to reduce the cost of PbS ink production from 16.9-35.5 \$ g^{-1} (PTLE method) to 5 \$ g^{-1}.[22]

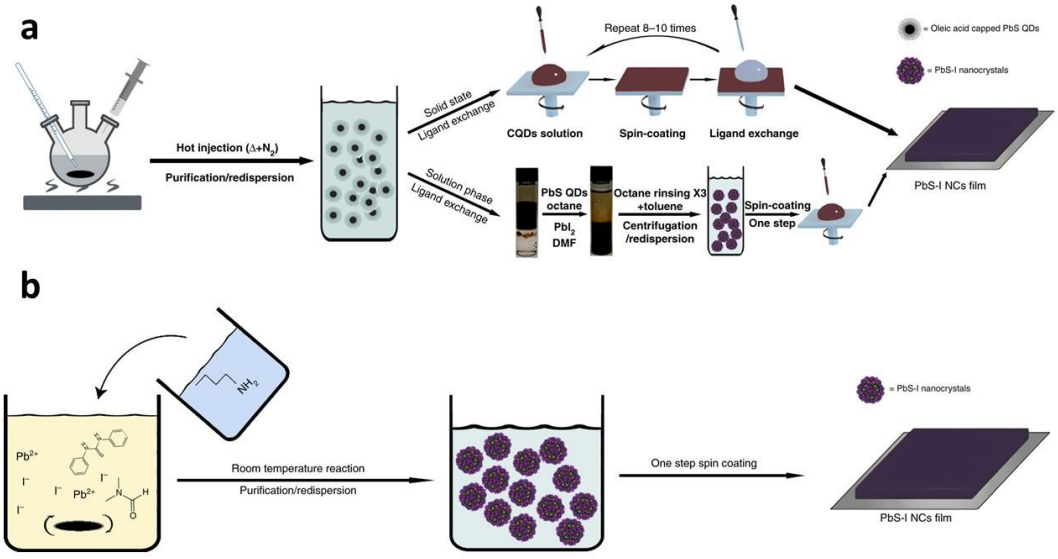

Figure 2.4. **a)** Representation of solid-state ligand exchange (L-B-L) and solution phase ligand exchange (PTLE). **b)** Representation of the direct synthesis PbS inkstrategy (DS-PbS ink).[23]

In DS method, PbI_2 and diphenylthiourea (DPhTA) can be used as the lead source and sulfur source, respectively, in combination with the injection of butylamine (BTA) into the reaction system. Under alkaline conditions, DPhTA was converted to thiol (-SH) group, which then reacted with PbI_2 to produce PbS colloidal quantum dots (CQDs) capped with ligands.[19] Additionally, BTA played a role in controlling the nucleation and growth of the CQDs, resulting in uniform-sized particles. The basic schematic of this method can be seen in Figure 2.4-b. This innovative synthesis method, can be performed at room temperature, has the potential to replace the traditional and complicated ligand exchange steps.

Detailed explanations about SSLE, PTLE (or SPLE) and DS method are given in the next sections of this chapter.

2.4.1 Solid State Ligand Exchange of PbS CQDs

In SSLE method, the PbS CQDs capped with long-chain OA ligands (synthesized PbS CQDs with hot injected method) are spin-coated on the device and ligands are exchanged by a layer by layer (L-B-L) approach. The CQD solid films were then soaked in a short-ligand solution for the ligand exchange, such as tetrabutylammonium iodide (TBAI), 1-ethyl-3-methylimidazolium iodide (EMII), or 3-mercaptopropionic acid (MPA).[24–26] To apply these shorter ligands, TBAI, EMII or MPA should be dissolved in solutions like acetonitrile (ACN) or methanol (MeOH). The L-B-L technique is mainly preferred for this ligand exchange method as discussed in previous section. Thus, after depositing the OA capped PbS CQDs, the short ligand solution is applied as seen in Figure 2.4-a. Generally, it is waited for 30-45 seconds for short ligands to alternate with long ligands and then the spin process is continued.[19,24] It is important to keep in mind that the surface ligands of CQDs might not entirely be replaced by the short ones, indicating that the SSLE process for the deposition of CQD solid films would not be able to effectively passivate the surface defects of CQDs.[19] To have a better PbS CQD film quality in terms of defect densities and passivation, the PTLE technique (which allows PbS ink production) can be a good alternative.

2.4.2 Phase Transfer Ligand Exchange and PbS Ink

In the PTLE technique, unlike SSLE, ligand exchange occurs in the liquid phase, and PbS colloidal quantum dots (CQDs) surrounded by PbI_2 are obtained in an ink form. This enables the production of PbS ink, which can be directly coated onto substrates in a single step. During the preparation of colloidal quantum dot (CQD) inks, lead halides, specifically PbI_2 and $PbBr_2$, were utilized as ligands to substitute the oleic acid (OA) ligands present on the surface of the dots. As represented in Figure 2.4-a, dimethylformamide (DMF), which dissolved PbX_2 (where X represents I and Br), was introduced into the octane solution containing OA-capped CQDs. Through

vigorous stirring of the mixture, the PbS CQDs underwent a phase transfer from the non-polar phase (octane) to the polar phase (DMF), resulting in the formation of halide capped CQDs. The presence of a double layer consisting of PbX_3^-, NH_4^+, and PbX^+ on the dot surface facilitated the uniform dispersion of CQDs within the polar DMF solvent, thereby maintaining the colloidal system. Finally, the CQD powder was collected and dispersed in various polar solvents, such as DMF, chlorobenzene, and BTA, thereby forming the CQD inks.[19] Since this method allows one-step deposition and offers reduced trap states and defects, it is considered as a more convenient process as compared to the SSLE technique.

2.4.3 Direct Synthesis of PbS Ink

Direct synthesis (DS) is a one-step method to obtain low-cost PbS CQD ink for optoelectronic applications. The resulted ink, called direct synthesis PbS ink (DS PbS ink), can be directly applied to optoelectronic device fabrication processes without complex ligand exchange mechanisms.[22,27] DS method obeys LaMer and Dinegar as hot injection synthesis. Firstly, the reaction begins with induction period where the precursors react to form monomer. It generally takes 0-45 seconds. The second step is the nucleation stage, where the nucleation begins to form nuclei as the concentration of monomer approaches the critical concentration. Then it goes to the final step known as growth stage. The growth of nuclei commences through the assimilation of monomers, leading to the formation of the ultimate colloidal quantum dots (QDs).[27] It was reported that PbI_2 possess too low reactivity to react with DPhTA sulfur source.[27] Yet, mixing PbI_2 with a polar solvent like DMF was reported as a strategy to activate PbI_2 and trigger the reaction.[27] Thus, the following chemical reactions was suggested for the DS PbS ink method.[27,28]

$$PbI_2 + X\ (Polar\ Solvent) \rightarrow [PbI_mX_n]^{2-m}$$

$$[PbI_mX_n]^{2-m} + Sulfide\ Precursor \rightarrow PbS\ CQD\ Ink$$

For the $[PbI_m X_n]^{(2-m)}$ term, the reactivity increases as the value of m increasesPbI_3^- and PbI_4^- show higher reactivity as compared to PbI_2.[27,29]

PbI_2 functions as a dynamic reservoir that releases the active Pb precursor $[PbI_m]^{2-m}$ ($m > 2$) in a controlled manner. Hence, the key step here is the dynamic conversion of PbI_2 to observe controlled nucleation and growth steps as explained. In a typical DS method for PbS CQD ink, PbI_2 and BTA are dissolved in a polar solvent which is generally chosen as DMF. After arranging and stabilizing the temperature of the solution for the intended CQD size, DPhTA can be injected to the Pb solution. Growth time of the reaction depends on the temperature and the concentration of DPhTA and PbI_2. After purification steps, obtained PbS CQD powder can be redissolved in DMF and can be deposited onto the device as ink form as represented in Figure 2.4-b.[27] Nevertheless, this synthesis method is still in the process of optimization and has potential for further optimizations.

2.5 Photodiodes

Photodiodes are considered as a type of photodetector that consists of semiconductor materials and are able to convert incident light into the electrical current. According to its design (p-n, PIN junction) spectrum response window width (broadband, panchromatic, or narrowband, wavelength selective), or the type of semiconductors they use (organic, inorganic, or hybrid), photodiodes can be categorized in a number of different ways.[30] These type of photodetectors have large application areas such as information technology, optical biological sensors, SWIR imagers etc.[30] In numerous applications, there is a demand for high speed and optimal signal-to-noise ratio performance. Consequently, it is imperative for the system to possess specific characteristics, namely low dark current and noise levels, high quantum efficiency, elevated responsivity, and rapid response time.[31] Due to the numerous experimental factors that must be taken into consideration, measuring detector parameters is a challenging task.[31] It is crucial to carefully regulate a number of electrical and radiometric parameters, and these parameters must be handled concurrently. In this

thesis the main photodiode structure is the PIN photodiode structure where PbS CQDs act as an active material. The working principle of PIN photodiodes is discussed in the next section.

2.5.1 Working Principle of PIN Photodiodes

All photodiodes share the same working principles. In contemporary technology, the p-n junction is considered as a fundamental component for the most of semiconductor devices such as light emitting diodes, lasers, and transistors. A significant majority of fabricated photodiodes consists of at least one junction between semiconductor regions oppositely doped. It indicates that it is crucial to obtain proper p-n junction for a high-performance photodiode.[32]

The joining of a p-type semiconductor (in which the majority of charge carriers are holes, and the minority are free electrons) and an n-type semiconductor (in which the majority of charge carriers are free electrons, and the minority are holes) is referred to as a p-n junction. The p-n junction is the intersection of these two separate semiconductor areas, where both p- and n-type materials are present. In p-n junction, an area called depletion region is formed due to the diffusion of electrons from the n-type semiconductor layer to the p-type semiconductor layer as seen in Figure 2.5-a. No free carriers exist within this depletion region. This situation causes a built-in voltage to create an electric field across the depletion region. Consequently, current is able to only flow in one direction from anode to cathode. Applying forward bias to a photodiode might be possible but the current generation occurs in the opposite direction. This is why most photodiodes are reversed biased. Moreover, some photodiodes cannot be exposed forward biased without damage.[33] The working mechanism of photodiodes relies on the photoelectric effect. If the incident photon onto the device has enough energy it can release an electron from the atom which creates electron-hole (e^- and h^+) pairs in the depletion region. Electrons move toward the positive potential (cathode) whereas the holes move to the negative potential (anode). This movement creates current which is called as photocurrent.[33]

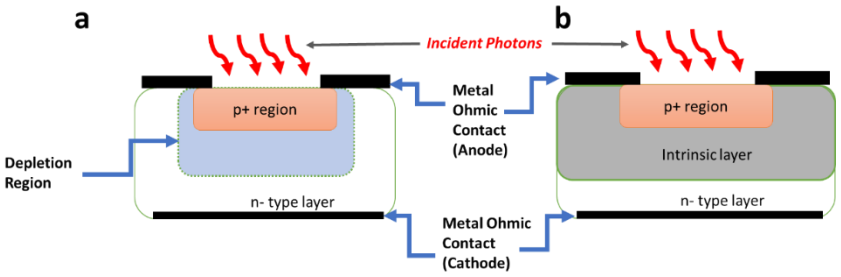

Figure 2.5. **a)** Cross section of a p-n photodiode **b)** Cross section of a PIN photodiode.

The PIN photodiodes are very similar to the p-n photodiodes with one major difference. Instead of combining the p and n layers to obtain depletion region, an intrinsic layer is placed in this structure as seen in Figure 2.5-b. Under an appropriate reverse bias, the intrinsic layer in PIN structure can be occupied by depletion region completely which means greater depletion region.[31] Generally, the p and n type semiconductors have higher energy gap in this structure so the incident light can only be absorbed from intrinsic material.[31] Thus, the e^- and h^+ pairs are only produced within intrinsic layer. The movement of h^+ and e^- pairs and schematic of band diagram of PIN photodiodes can be seen in Figure 2.6. The main advantage of PIN photodiode compared to p-n photodiode is high response speed since the depletion region is larger.[33]

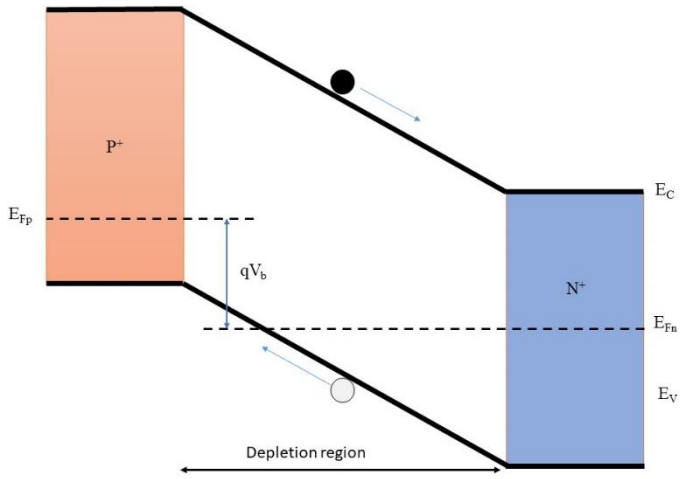

Figure 2.6. The band diagram of P-I-N photodiode under zero bias.

2.5.2 Figures of Merit for Photodiodes

There are several important figures of merit for photodiodes: dark current (I_{dark}), external quantum efficiency (EQE), noise equivalent power (NEP), specific detectivity (D*), and response time (τ).

2.5.2.1 Dark Current

Dark Current (I_{dark}) represents the constant current that can be observed under dark conditions. Eventough the photodiode is operated under reverse biased, a small saturation current ($I_{saturation}$) can be observed where $I_{saturation}$ shows the maximum current when forward bias is applied.[31] The dark current can be calculated by using the following formula:

$$I_{dark} = I_{saturation}[\exp\left(\frac{qV}{\beta kT}\right) - 1]$$

where q represents electron charge, β is the ideality factor of the junction, k is the Boltzman constant, V is the voltage and T is the temperature.

There are several main sources of I_{dark} such as generation-recombination current, trap-to-band mechanism, and surface or leakage current.[31]

2.5.2.2 External Quantum Efficiency

External Quantum Efficiency (EQE) is determined by taking the ratio of the quantity of charge carriers produced within the device to the quantity of photons that strike it. The relationship between responsivity and EQE can be seen in the following formula:

$$EQE(\lambda) = \frac{R(\lambda)hc}{q\lambda} \approx \frac{1.24R(\lambda)}{\lambda}$$

where R(λ) is responsivity, c is the velocity of light (write the numerical value and units), and λ is the wavelength of light. hc/q term in this equation can be approximated to be 1.24 when λ is in μm ($h = 6.6 \times 10^{-34}$ $m^2kg.s^{-1}$ and $q = 1.602 \times 10^{-19}$C.[34]

2.5.2.3 Noise Equivalent Power

Noise Equivalent Power (NEP) refers to the smallest detectable power level. NEP(λ) specifically refers to the optical power at which the signal-to-noise ratio (SNR) reaches unity. NEP can be found by the following formula:

$$NEP\ (\lambda) = \frac{\sqrt{< I_n^2 >}}{R(\lambda)}$$

Where Δf is detection bandwidth and $<I_n>$ represents the cumulative noise current and R represents the responsivity. The cumulative noise current comprises various noise origins, encompassing shot noise from dark current (I_{sh}), thermal noise (I_{th}), and and low-frequency flicker noise (1/f). The unit of NEP(λ) is W $Hz^{0.5}$.[34]

Under an applied reverse bias, the noise current is dominated by the shot noise which is dominated by the dark current.[35] Thus, one can show the noise dark current as follows:

$$I_n \sim \sqrt{2qI_{dark}\Delta f}$$

Where Δf is detection bandwidth and q is the electrical charge.

Moreover, SNR parameter is also important for photodiodes since it shows the quality of signal. To achieve a high SNR, the low noise and high responsivity values are required.

2.5.2.4 Specific Detectivity

Specific Detectivity (D*) is the primary performace indicator therefore figure of merit for the photodiodes, allowing the comparison of different photodiode devices that have different configurations and areas. D* represents the signal-to-noise raito (SNR) in an alternating current (a.c.) signal when the detector is exposed to an 1 W optical power, 1 Hz noise bandwidth and the detection area is 1 cm^2. Value of D* is directly proportional to the responsivity of the photodiode.[34] The value of D* (in units of $Hz^{0.5}$ W^{-1} also called Jones (J)) can be obtained from the following formula:

$$D^*(\lambda) = \frac{\sqrt{A\Delta f}}{NEP} = \frac{R(\lambda)\sqrt{A\Delta f}}{< I_n >} = \frac{q\lambda\sqrt{A\Delta f}\,EQE}{hc\,I_n}$$

where A is representing the area of device.[34]

2.5.2.5 Response Time

Response time or time constant (τ) is representing the duration it takes for output signal of a photodiode to reach approximately 63% ($1-e^{-1} \approx 63\%$) of its peak steady-state value when it is exposed to an incident optical signal.[34]

τ is also defined as the time for the signal to rise 10% to 90% (rise time (RT)) or fall from 90% to 10% (fall time (FT)) of the final value. τ can be calculated by the following equation:

$$\tau = \frac{1}{2\pi f_{3dB}}$$

where f_{3dB} 3 dB or cut-off frequency of device.

The equation is used to calculate the minimum rise time and 3 dB bandwidth in electrical and electro-optical systems. It was demonstrated that the combination of equations for the frequency- and time-dependent responses of a perfect RC low-pass filter circuit leads to this expression. The correctness of the numbers derived using the mathematical expression connecting rise time and 3 dB frequency depends on how closely the response of the system under investigation resembles that of an ideal RC low-pass circuit. [31]

The p-n junction in photodiode detectors functions as an obstacle for the movement of majority carriers, thereby inhibiting the replenishment process. Due to the fact that the carrier transit time, which refers to the duration it takes for charge carriers to cross the high-field region of the junction, can be considerably shorter than the lifespan of the carriers, the response time is greatly improved.

2.6 PbS CQD Photodiodes for SWIR Detection

Nowadays, SWIR detection has received great attention for many fields such as food inspection, remote sensing, autonomous driving and image capturing. Sensor bands are utilized to carefully choose specific regions of the electromagnetic spectrum. This selection is aimed at optimizing the collection of data pertaining to particular categories of information. This optimization is particularly noticeable in the short-wave infrared (SWIR) (0.9-2.5μm), mid-wave infrared (MWIR) (3-5μm), and long-wave infrared (LWIR) (7.5-10.5μm) regions.[36]

Moreover, silicon-based complementary metal-oxide semiconductors (CMOS) are especially crucial for imagers since they are able to convert photocurrent into the digital signals which can create digital images.[37]

Indium Gallium Arsenide (InGaAs) is still dominant in the market eventough it requires hybrid packaging and has high cost. However, PbS CQDs can be monolithicily deposited onto the CMOS ROICs because of its solution processibility.[38] In addition to that, PbS CQDs can absorb the light from the wavelength 200 nm to the wavelength 2300 nm by the correct size arrangment.[34]

Thus, PbS CQDs based photodiodes have gained significant attention due to their simple, cost-effective, and solution-based manufacturing techniques.

2.7 Device Architecture of PbS CQD Photodiodes

Device architecture in PbS CQD based photodiodes is playing a key role as ligand exchange mechanism or synthesis method since the performance of device is also mainly based on bandgap engineering. There are many possible ways to construct a PbS CQD based photodiode. In this study the PIN structure is chosen to produce this type of photodiode. To achieve a working photodiode device, there must be certain layers. It can be built from top to bottom as follows: top contact layer, electron transport layer (ETL) which is n-type semiconductor as described in previous section, active layer, hole transport layer (HTL) which is p-type semiconductor as described in previous section and bottom contact layer. In this study the device architecture is chosen as follows: Indium Tin Oxide (ITO) as the top contact layer, zinc oxide (ZnO) as the ETL, PbS CQD INK as an intrinsic layer, PbS-EDT as the HTL and gold (Au) as the bottom contact layer (see Figure 2.7-a).

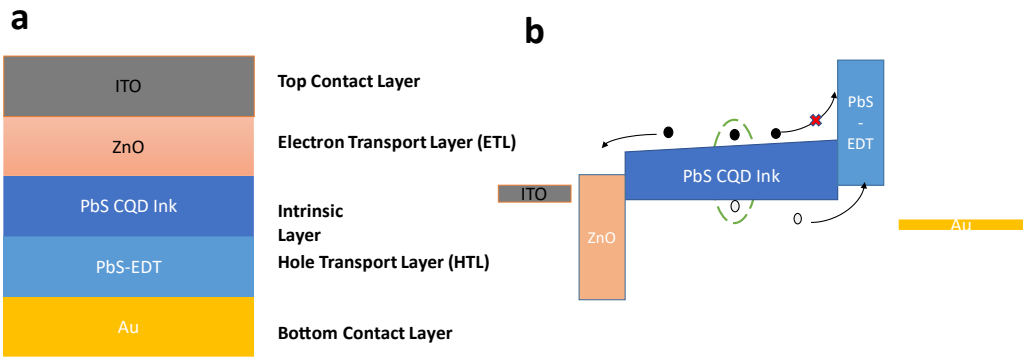

Figure 2.7. **a)** Device architecture of a PbS CQD based photodiode and **b)** working principle of photodiode based on its energy bandgap in eV.

As represented in Figure 2.7-b, in this architecture, electron-hole pairs are generated in PbS CQD Ink layer. On the other hand, holes and electrons are collected from Au and ITO layers, respectively. The generated electrons are able to move to the ZnO side, but they are unable to move towards the PbS-EDT side due to the presence of an energy barrier

There are other architecture possibilities for PbS CQD based photodiodes. The change in device architecture leads to differences in device performances. In the literature, it is possible to find many studies that contain different device architecture and device performance. Summary of the state of art photodiodes based on PbS CQDs can be seen in Table 2.1.

Table 2.1. Summary of the photodetector performance parameters of the state of art PbS CQD based photodiodes.

Architecture	**D*(Jones) @ λ (nm)**	**J_D (mA.cm^{-2})**	**EQE (%) @ λ (nm)**	**Bias (V)**	**RT/ FT (µs) @ 0V**	**Area (cm^2)**	**Ligand Exchange Mechanism**	**Ref. Year**
ITO/ZnO/PbS Ink/PbS-EDT/Au	6.710^{12} @980	2.9×10^{-5}	50 @980	−1	-	0.02	PTLE	Jung et. al., 2022 [39]
ITO/NiO/PbS-CQD/ZnO/Al	10^{12} @1800	2.9×10^{-3}	15 @1800	−0.5	11.0 /15.0	-	SSLE	Lee et. al., 2020 [17]
ITO/ZnO/C_{60}/PbS Ink/PbS-EDT/NiO/Au	1.5×10^{11} @970	1.78×10^{-6}	63 @970	−0.5	0.49/1 .15	$15x10^{-8}$	PTLE	Liu et. al., 2022 [40]
ITO/ZnO/ PbS Ink/PbS-MPA/PDBD-T/MoO_x/Ag	4.08 $\times 10^{11}$ @1300	2.0×10^{-3}	70 % @1300	−0.8	3.29/1 5.25	-	DS	Liu et. al., 2022 [27]
ZnO/PbS-TBAI/PbS-BDT/NiO	1.5×10^{11} @2100	2.5×10^{-2}	25 % @2100	−2	43/70	-	SSLE	Dong et al., 2019 [41]
ITO/PbS-EDT/PbS Ink/ZnO/Si	4.08×10^{11} @1490	4×10^{-4}	18 % @1490	−0.25	47.6/0 .8	0.05	PTLE	Xiao et al., 2020 [42]
ITO/PbS-TBAI/SiN/p-Si/Au	7.74×10^{10} @1064	6×10^{-3}	27.5 % @1064	0.05	160 / 320	0.25	SSLE	Wang et al., 2022 [43]
ITO/ZnO/PbS-TBAI/Si	5×10^{10} @1230	6×10^{-2}	14 % @1230	0	-	0.049	SSLE	Masala et al., 2015 [44]
ITO/ZnO/PbS Ink/ PbS-EDT/Au	2.34×10^{11} @980	4.36×10^{-3}	35.02 % @980	-0.5	2.04/3 .66	0.045	PTLE	This Thesis
ITO/ZnO/PbS Ink/ PbS-EDT/Au	5.23×10^{11} @980	7.6×10^{-4}	32.64 % @980	-0.5 0	6.15/ 18.02	0.045	DS	This Thesis
ITO/ZnO/PbS Ink/ PbS-EDT/Au	1.5×10^{13} @920	1.96×10^{-8}	35.19@ 920	-0.5	1.65/ 8.08	0.045	DS (Optimized)	This Thesis

According to Table 2.1, the ligand exchange mechanism and device architecture are the key parameters for manipulating the dark current density, EQE and D* parameters in a device. As seen in Table 2.1, the SSLE method is leading to a high dark current density (J_D) in the range of 10^{-2} to 10^{-3} mA.cm^{-2} as compared to a similar device architecture where it is reported to be as low as 10^{-6} mA.cm^{-2}.

Among the reasons leading to high dark current, it is known that trap bands caused by defects on the quantum dot surface and various interfaces in the detector's active layer are the main contributors, including interface-induced trap bands.[39,45] In addition to the increase in interface-induced dark current, quantum dots can fuse with each other and form dimers during synthesis, purification, and ligand exchange stages.[46] This phenomenon affects the optoelectronic properties of the device and leads to an increase in dark current. The problem of dimerization or fusion of CQDs is more pronounced in the SSLE method, where the ligand exchange procedure is longer and more laborious because of the old-fashioned L-B-L deposition technique.[46] Techniques such as PTLE and DS, which enable single-step coating, can further reduce dark current density to around 10^{-8} mA.cm^{-2} (see Table 2.1). Unlike SSLE, these methods involve ligand exchange in the liquid phase, which eliminates the interface issue in the active layer and reduces the occurrence of dimerization for quantum dots. Therefore, the devices that are made with PTLE shows better performance in terms of dark current density and detectivity whereas DS method is still its infantile stage.[27]

2.8 SCAPS 1-D Simulation

The numerical analysis was conducted in SCAPS-1D tool for one-dimensional simulations, developed by Department of Electronics and Information Systems (ELIS) of the University of Gent, Belgium.[47] Utilizing the SCAPS-1D simulation tool, one can compute current/voltage characteristics, photovoltaic parameters, quantum efficiencies, dopant density profiles, total generation/recombination profiles, along with corresponding energy band diagrams, among other factors. The tool operates on the principles of the one-dimensional Poisson's equation in semiconductors, carrier continuity (electron/hole transport), and the drift-diffusion differential equations.[48] Poisson's equation and continuity relations for holes and electrons as follows:

$$\frac{d}{dx}\left(\varepsilon(x)\frac{d\psi}{dx}\right) = q[p(x) - n(x) + N_{D^+}(x) - N_{A^-}(x) + p_t(x) - n_t(x)]$$

$$\frac{1}{j}\frac{dJ_n}{dx} + R_n(x) - G(x) = 0$$

$$\frac{1}{j}\frac{dJ_p}{dx} + R_p(x) - G(x) = 0$$

Here, ε(x) denotes the permittivity at the position within the device x, while ψ and q represent the electrostatic potential and electron charge. Symbols n and p signify the concentrations of free electrons and holes, and N^+_D and N^+_A represent the ionized concentrations of donor-like and acceptor-like dopants. Additionally, n_t and p_t denote trapped electrons and holes, J_n and J_p are the current densities of electrons and holes, G(x) represents the photogeneration rate, and $R_n(x)$ and $R_p(x)$ are defined as the electron and hole recombination rates, respectively. Details of the SCAPs parameters utilized in this thesis study are given in section 4.2 and 4.9.

CHAPTER 3

EXPERIMENTAL

3.1 Materials

Unless otherwise indicated, all chemicals utilized were of the utmost purity attainable and employed in their original form. Furthermore, all solvents employed were thoroughly dehydrated and utilized without any modifications.

Lead(II) oxide, (PbO, 99.999%, Aldrich), oleic acid (OA, 90%, Aldrich), 1-octadecene (ODE, 90%, Aldrich), hexamethyldisilathiane ($(TMS)_2S$, Aldrich), hexane (99%, Aldrich), acetone (99.8%, Acros Organics), methanol (99.8%, Aldrich), octane (99%, Aldrich), 1,2-ethanedithiol (EDT, 98%, Aldrich), acetonitrile (ACN, 99.8%, Aldrich), butanol (99.8%, Aldrich), hexylamine (99.0%, Aldrich), amylamine (99%, Aldrich), N,N-dimethylformamide (99.8% Aldrich), toluene (99.8%, Aldrich), 2-propanol (99.5%, Aldrich), diphenylthiourea (98%, Eastman), lead(II) iodide (99%, Aldrich), lead(II) bromide (98%, Aldrich), chloroform (≥99%, Aldrich), zinc acetate dihydrate ((≥99%, Aldrich), potassium hydroxide (≥90%, Aldrich).

3.2 Synthesis and Ink Preparation

The process of creating PbS CQDs and ZnO NPs involved utilizing the hot injection nanoparticle synthesis method with air-free Schlenk line techniques. The purification of the CQDs took place within a glove box (GB) filled with nitrogen gas. The PbS CQD ink is also prepared under inert environment.

3.2.1 ZnO NP Synthesis via Hot Injection Method

For the ZnO ETL layer, a modified literature method was followed.[27] Firstly, a three-neck reaction flask was connected to a condenser to establish a reflux system, Zinc acetate dihydrate ($Zn(CH_3COO)\cdot_2H_2O$), abbreviated as (ZnAC), was used as the source of zinc. 1.475 g (6.720 mmol) of ZnAC in dihydrate form is dissolved in the three-neck reaction flask using 62.5 mL of methanol (MeOH). Next, 0.740 g (13.19 mmol) of potassium hydroxide (KOH) is dissolved in a clean Erlenmeyer flask using 32.5 mL of MeOH. The potassium hydroxide solution is then added dropwise to the zinc acetate solution using a needle for 15 minutes, and the solution is stirred at 60ºC for 2.5 hours using a magnetic stirrer. ZnO nanoparticles are extracted from the solution by centrifugation (5000 rpm, 5 minutes). The nanoparticles are washed twice with MeOH and centrifuged again (5000 rpm, 5 minutes). Finally, a mixture of chloroform and MeOH in a 1:1 volume ratio is added to the centrifuged precipitate, and the solution is filtered through a 0.45-micron filter.

3.2.2 PbS CQD Synthesis via Hot Injection Method and PbS CQD Ink Preparation by PTLE Approach

PbS quantum dots (QDs) with a bandgap of 1.3 eV were synthesized using a modified method described in the literature.[16] PbS CQDs were synthesized using a Schlenk line system with a two-way flow mechanism.

In the synthesis of PbS CQDs with a bandgap of 1.3 eV, 0.4528 g (2.030 mmol) of lead oxide (PbO) was dissolved in a mixture of 1.51 mL (4.784 mmol) of oleic acid (OA) and 17.99 mL of octadecene (ODE). Then, a three-neck reaction flask was attached to the Schlenk line, and the mixture was stirred under vacuum with a magnetic stirrer until it reached 100 ºC. The reaction continued at this temperature for an additional 2 hours once it reached 100 degrees Celsius. This step helped remove the remaining water under vacuum and eliminated acetic acid produced as a result of the reaction between PbO and OA. Meanwhile, the lead oxide in the reaction

flask completely dissolved, forming Pb (lead) - Oleic acid (OA) complexes. The color of the resulting complex solution changing from yellow to transparent (as in Figure 3.1-a) indicates this transformation. After 2 hours, the reaction flask is placed under nitrogen again and heated to 160 ºC (coordination temperature). It is then cooled down to 125 ºC (injection temperature) to reach the desired temperature for injection. Next, 0.21 mL of bis-trimethylsilyl sulfide $(TMS)_2S$ is dissolved in 10 mL of octadecene (ODE) as the sulfur precursor. This prepared solution is quickly injected into the reaction flask using a needle at 125 ºC. The rapid injection is crucial to obtain a product with uniform distribution. The color of the solution changed from transparent to black as shown in Figure 3.1-a and Figure 3.1-b. After waiting for 20 seconds (the growth time of the quantum dots), ice is placed under the reaction flask to cool the setup and allow it to reach room temperature for over a few minutes. During this time, the temperature is monitored using a digital thermometer. Then, the synthesis formed in the reaction flask is transferred to a transfer flask using a cannula for further conditioning in a glove box system filled with nitrogen.

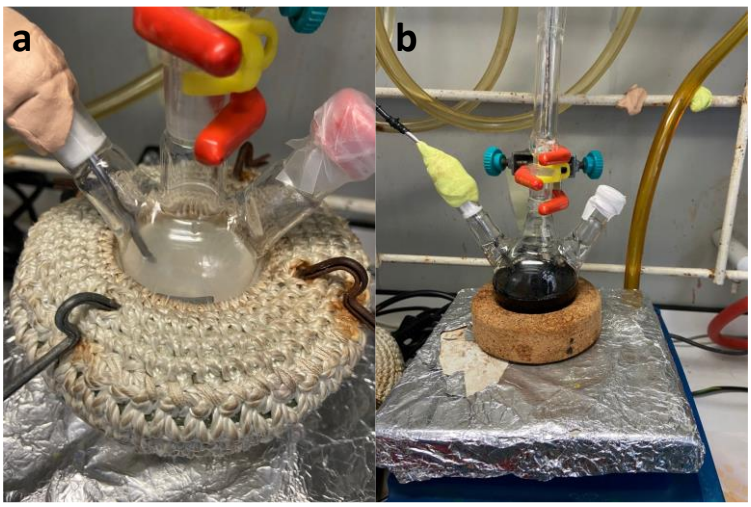

Figure 3.1. **a)** Before injection. **b)** After injection.

After transferring the entire synthesis to the transfer flask, the purification stage is initiated. The purpose of the purification process is to remove any unreacted OA

chains and ODE from the solution. The CQDs obtained were subjected to purification twice using a solvent/anti-solvent pair of hexane/acetone, followed by centrifugation at 5000 rpm for 5 minutes. In the first step, a mixture of hexane/acetone in a ratio of 1:4 was used, and in the second step, a mixture of hexane/acetone in a ratio of 1:1 was employed. The precipitate obtained after vacuum drying was dispersed in octane and then filtered through a 0.22 μm PTFE syringe filter. This filtration process is carried out for photodiode applications and subsequent characterization steps.

After the hot injection synthesis, the PbS CQD ink can be prepared. Firstly, the precursor solution of lead halides was prepared by dissolving 100 mM PbI_2, 40 mM $PbBr_2$, and 60 mM ammonium acetate in DMF (dimethylformamide). Droplets of PbS quantum dots (CQDs) with a bandgap of 1.3 eV, surrounded by OA, were gradually added to the prepared and stirring ligand precursor. The solution was continuously stirred for 5 minutes after the completion of CQD addition. At the end of 5 minutes, phase separation occurred, with a transparent solution appearing on the upper side and a black solution observed on the lower side, indicating the presence of two phases. Then, the CQDs in the DMF phase were washed three times with octane and subsequently precipitated using toluene. After centrifugation, the CQDs were separated and dried under vacuum for 30 minutes, resulting in the synthesis of PbS CQD solid surrounded by PbI_2 in powder form. Precipitated CQDs were collected using butylamine (200 mg/mL). All of these procedures were carried out within a glove box system conditioned with nitrogen to prevent material oxidation.

3.2.3 Direct Synthesis of PbS CQD Ink

Direct Synthesis of PbS CQD ink was adopted from the literature.[22,23,27,49] A solution containing 0.06 mmol of PbI_2 and 1 mL of butylamine was dissolved in 8 mL of DMF while being stirred under a nitrogen atmosphere. Prior to injecting the DPhTA solution, the temperature of the Pb solution was adjusted to 25 ºC to achieve the desired size of the quantum dots. When the temperature stabilized, 1 mmol DPhTA

in 1 mL of DMF was rapidly injected into the Pb solution. To achieve the desired size enlargement of the quantum dots, the reaction and stirring process were conducted for 10 minutes. Following the reaction, the quantum dots were separated by precipitating them using toluene as an anti-solvent. The mixture was then subjected to centrifugation at 8000 rpm for 5 minutes. After centrifugation, the CQDs were dissolved in DMF for the purpose of device fabrication.

3.3 Material Characterization / Instrumentation

3.3.1 Absorption Spectroscopy

The absorption characteristics of quantum dots were evaluated in two distinct configurations: as a suspension in tetrachloroethylene (TCE) within a tightly sealed quartz cuvette or as a thin film coating on substrates made of quartz or glass. The measurements were performed using Shimadzu 3600 plus UV-Vis-NIR spectroscopy system, enabling precise spectral data acquisition. To ensure an environment devoid of reactive influences, the samples were meticulously prepared within the confines of a glove box filled with nitrogen gas, maintaining an inert atmosphere throughout the experimental process.

3.3.2 Transmission Electron Microscopy

Transmission electron microscopy (TEM) measurements were conducted in METU Central Lab by using a Jem Jeol 2100F 200kV high-resolution transmission electron microscope (HRTEM) equipped with a Schottky-type field emission gun as an electron source. The instrument operated at voltages ranging from 80-200 kV. For TEM imaging, samples were prepared by drop-casting a diluted solution of nanoparticles (NPs) in TCE onto 200 Mesh carbon-coated TEM grids. The solvent was allowed to evaporate at room temperature. A GATAN Orius SC10002 camera, serving as the CCD camera, was employed to capture the TEM images.

3.3.3 Fourier-transform Infrared Spectroscopy

The acquisition of Fourier-transform infrared (FTIR) spectra was performed in transmission mode utilizing an HYPERRION spectrometer, which had a resolution of 64. To prepare the samples for FTIR measurements, a dilute solution of nanoparticles was deposited via spin coating method onto quartz substrates. For background measurements, clean quartz substrates were used. Additionally, in the case of OA-capped or ligand exchanged nanoparticles, they were also deposited via spin coating method onto the quartz substrates prior to conducting the FTIR analysis.

3.3.4 Scanning Electron Microscopy

Scanning Electron Microscopy (SEM) imaging was performed by using Hitachi SU-8230 SEM that is located at METU MEMS CENTER's clean room.

3.3.5 Photoluminescence

Photoluminescence (PL) was performed via Horiba Jobin Yvon fluorolog-3 measurement system which contains Hamamatsu NIR Photomultiplier Tube Module Controller which is located at Bilkent University UNAM Lab. Unless otherwise noted, the measurements were carried out by Firdevs Aydın. The quantum dots were excited via 500 nm light.

3.4 Photodiode Simulation

Device architecture is one of the most important parameters that affects the performance of device as discussed in 2.6.1. It has great influence on EQE, detectivity, and dark current. To achieve optimum parameters the Solar Cell Capacitance Simulator (SCAPS) was used. Experiments have been conducted in SCAPS software for determining the arrangement sequences of layer structures in

device architecture in accordance with the direction of incident light. The parameters required for simulating the layers have been obtained from previous studies in the literature, and they have been further modified for the device architecture within the scope of this thesis. The parameters that are used for SCAPS simulation can be seen in Table 3.1. The electron and hole thermal velocities were set at 10^7 cm/s for all layers. With these parameters, I-V measurement simulation, and quantum efficiency measurement simulation. In the first simulation scenario, the device is illuminated from ZnO side (top illuminated) to construct P-I-N structure. In the second simulation scenario, the device is illuminated from PbS-EDT side (bottom illuminated) in order to construct N-I-P photodiode structure. The aim is to decide which type of structure offers a better performance in terms of quantum efficiency and I-V characteristics. The detail of the simulation is discussed in section 4.1.

Table 3.1. The basic SCAPS parameters for ZnO, PbS Ink and PbS-EDT layers.

	ZnO [40]	**PbS Ink** [40]	**PbS-EDT** [50]
Thickness (nm)	100	350	60
Bandgap (eV)	3.50	1.3	1.31
Electron affinity (eV)	4.00	4.00	3.90
Dielectric permittivity	8.00	20.00	18.00
CB effective density (cm^{-3})	10^{18}	10^{18}	10^{19}
VB effective density (cm^{-3})	10^{18}	10^{19}	10^{19}
Electron mobility ($cm^2/V{\cdot}s$)	20.00	0.005	$2.32{\cdot}10^{-4}$
Hole mobility ($cm^2/V{\cdot}s$)	20.00	0.005	$4.64{\cdot}10^{-3}$
Shallow uniform donor density ND (cm^{-3})	10^{17}	0	10^{14}
Shallow uniform acceptor density NA (cm^{-3})	0	10^{16}	$3.71{\cdot}10^{16}$

3.5 Photodiode Fabrication

Figure 3.2 visually presents the sequential stages entailed in the fabrication of photodiode. Commencing this process, glass substrates featuring a structured coating of indium tin oxide (ITO) were procured from Psiotec. A meticulously devised cleaning regimen ensued, encompassing a meticulous sonicating treatment in acetone, isopropyl alcohol, hellmanex III, and deionized water for a spun of 15 minutes. Subsequently, an expedient nitrogen stream was employed to expel any residual moisture from the substrates, which were then diligently placed within an oven at an elevated temperature of 100°C for no less than 3 hours. The ZnO layer was synthesized via hot injection method as NP form and the solution was deposited with spin coater onto the ITO substrates.

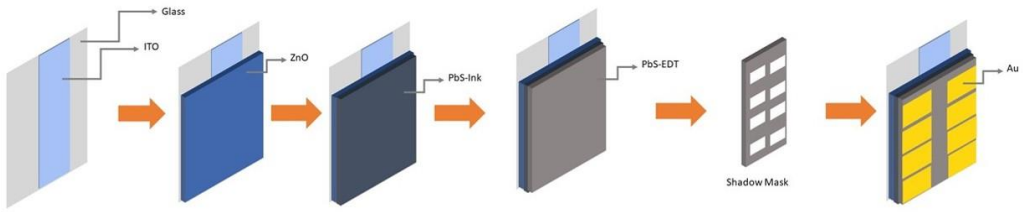

Figure 3.2. Schematic of the photodiode fabrication process.

After that, the active layer (PbS ink layer) was deposited by spin coating. Later, to obtain PbS-EDT layer, L-B-L technique was preferred. The schematic representation of the L-B-L method to produce PbS-EDT layer can be seen in Figure 3.3. Firstly, the EDT solution (0.02 v% in ACN) is applied onto the PbS ink layer, waited 30 seconds and then deposited at 2500 rpm for 10 seconds by spin coating which is followed by ACN rinsing. Then the oleate capped PbS CQD in octane (50 mg/mL) is applied with 5 seconds pause time and then deposited at 2500 rpm for 10 seconds. Then, EDT is deposited for ligand exchange. It is followed by again ACN rinsing. The same procedure is repeated from PbS CQD deposition step. The second layer

was the last layer in this procedure, and it is finalized with octane treatment to remove unexchanged quantum dots.

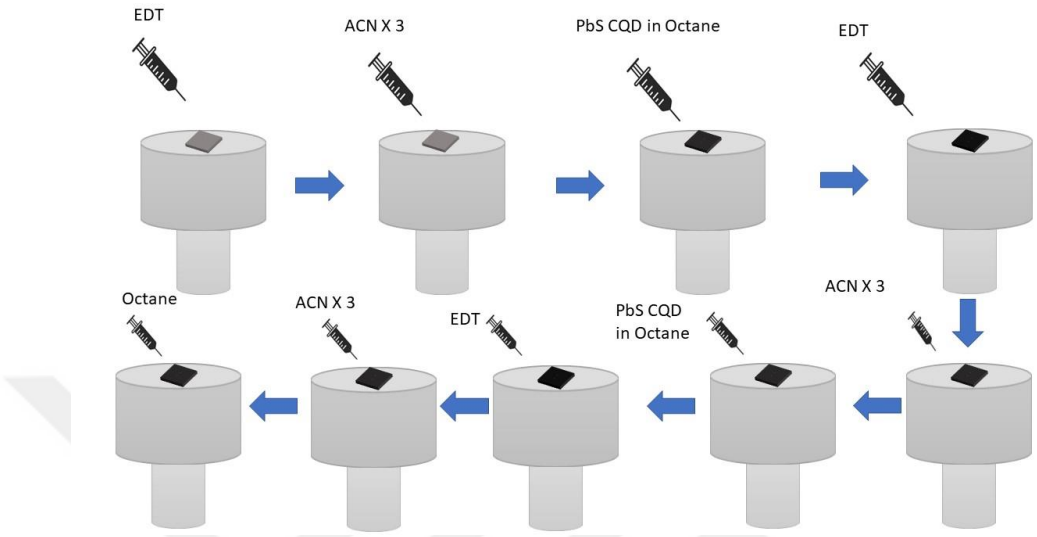

Figure 3.3. L-B-L technique for PbS-EDT layer.

Finally, the substrates are placed (with shadow mask) into the thermal evaporator for Au (65nm) evaporation at a pressure of 10^{-6} Torr. The active area (pixel size) is 4.5 mm^2. The produced photodiodes from both sides can be seen in Figure 3.4-a and Figure 3.4-b.

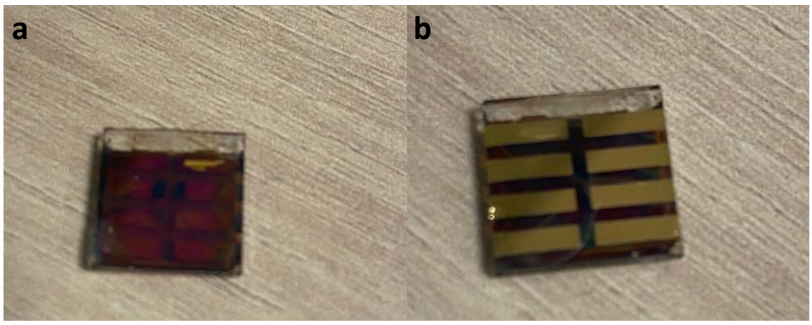

Figure 3.4. **a)** Top side of produced photodiode. **b)** Bottom side of produced photodiode.

3.6 Photodiode Characterization

3.6.1 Wire Bonding

Wire bonding is a technique to connect a semiconductor device to an IC and it is relatively low-cost procedure compared to flip chip bonding technique.[51] In this case, the fabricated PbS CQD based photodiodes were integrated into the printed circuit boards (PCB) by using F&K Delvotec Wedge 5630 system located at METU MEMS CENTER's test and characterization room.

Figure 3.5. F&K Delvotec Wedge 5630 wire bonding system.

As shown in Figure 3.5, the wire bond setup has one X-Y table with substrate carrier, microscope, keypad, and bond head /measuring head. Firstly, the gold contact locations were determined carefully. Then, they were bonded to proper contact points on PCBs. The locations of the contact points are determined by microscope. Then the ITO contact layer is bonded to the PCB. This method allowed contact from

top and bottom layers of the photodiode which is necessary to perform current-voltage, quantum efficiency and rise/fall time measurements. PbS CQD based photodiode device integrated into PCB can be seen in Figure 3.6-a.

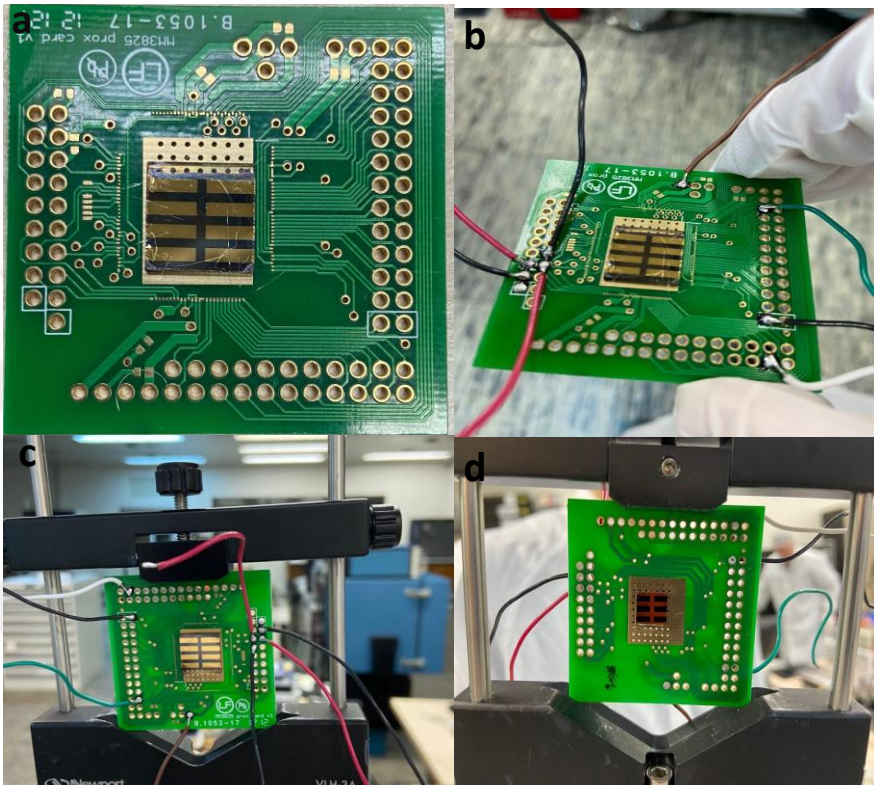

Figure 3.6. **a)** Photodiode after wire bonding. **b)** Photodiode after getting contact cable. **c)** Bottom side of photodiode. **d)** Top side (illuminated side) of photodiode.

To perform the measurements, it is necessary for the crocodile clips to make contact with the contact points. After the wire bonding process to establish the contacts, the cables need to be connected in a way that is suitable for the crocodile clips to make contact with the contact points on the PCB. This can be seen in Figure 3.6-b. The bottom part (the part with the gold layer) and the top side (illuminated side / ITO layer side) of the photodiode device are shown in Figure 3.6-c and Figure 3.6-d, respectively.

3.6.2 Current Voltage Measurement

Current voltage measurements were performed with Keithley 2425 device under dark and illuminated conditions. The used Keithley 2425 device and experiment setup can be seen in Figure 3.7-a and Figure 3.7-b, respectively. Voltage is applied from -1 V to 1 V with a 0.01 sweep voltage. The results are collected with Lab Tracer software.

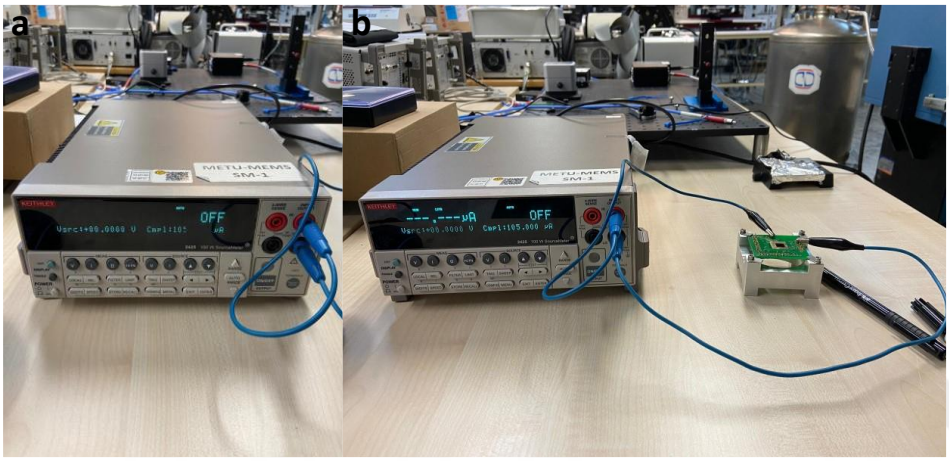

Figure 3.7. **a)** Keithley 2425 device, **b)** connection of the photodiode to the Keithley 2425.

3.6.3 External Quantum Efficiency Measurement

External quantum efficiency (EQE) was conducted at METU QD Lab located in the METU Chemistry Department by employing a Newport QUANTX-300 apparatus. Setup of the device can be seen in Figure 3.8-a. The measurements were performed outdoors at a temperature range of 20-28°C, maintaining a working distance of 85 mm. The measurements were carried out on photodiodes positioned on the printed circuit board (PCB) and secured to a test holder as in Figure 3.8-b. The incident white light, generated by a 100 W Xenon lamp, was filtered and its central wavelength was adjusted within a desired range using an Oriel Monochromator (CS130). For

calibration purposes in the 325-1800 nm range, a silicon-germanium detector (PN: 603621) was used as a reference detector, which had been calibrated at the Newport Research Center (NRC).

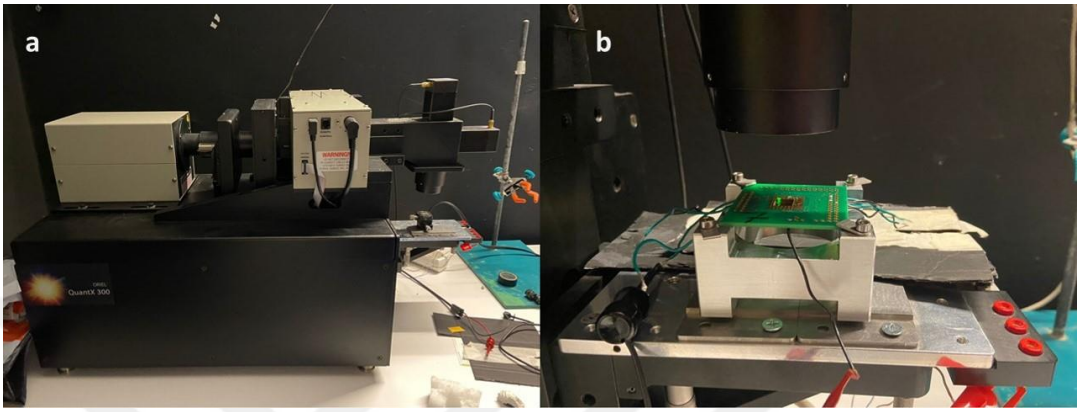

Figure 3.8. **a)** Newport QUANTX-300 external quantum efficiency measurement setup. **b)** On going measurement on a PbS CQD photodiode integrated into PCB.

3.6.4 Rise Time & Fall Time Measurement

Rise and fall time measurements for photodiodes were conducted at METU MEMS Center's test and characterizations area. To see the generated signal within the photodiode samples the Agilent MSO-X4034A Mixed Signal Oscilloscope is used as in Figure 3.9-a. To produce intended waveforms infrared LED is driven by Agilent 3322A 20 MHz function / arbitrary waveform generator is used as shown in Figure 3.9-b.

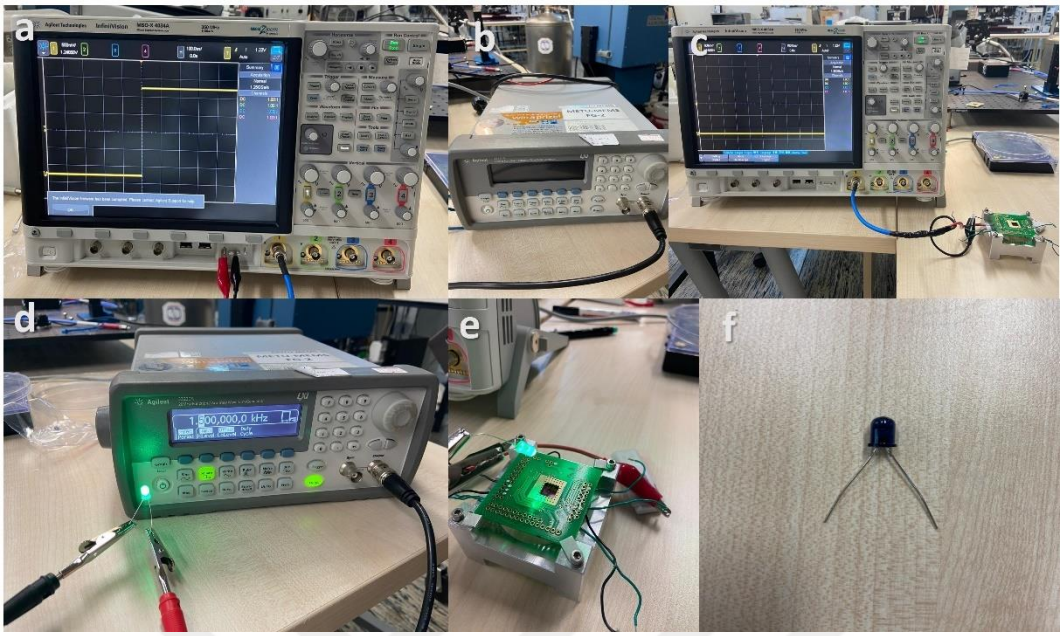

Figure 3.9. **a)** Agilent MSO-X4034A Mixed Signal Oscilloscope. **b)** Agilent 3322A 20 MHz function / arbitrary waveform generator. **c)** The connection of a sample to the oscilloscope. **d)** Validating the signal via green LED. **e)** Shining green LED onto the sample to control the parameters. **f)** TSAL6200 GaAlAs 940nm high-power infrared LED.

Initially, the photodiode structure is positioned onto the sample holder. Subsequently, the photodiode's contact is linked to the oscilloscope, as illustrated in Figure 3.9-c. Simultaneously, a green LED is attached to the waveform generator to validate the presence of the signal, depicted in Figure 3.9-d. Correspondingly, the photodiode device is exposed to the emitted light from the green LED as Figure 3.9-e, facilitating real-time assessment of wave parameters such as frequency, aided by the oscilloscope. Following this, the green LED is replaced by the TSAL6200 GaAlAs 940nm high-power infrared LED for carrying out the actual measurements as shown in Figure 3.9-f.

3.6.5 Capacitance-Voltage (C-V) Measurement

Capacitance-voltage measurements conducted within METU MEMS Center's test and characterizations area. To make C-V analysis, Agilent E4980A 20Hz-2MHz Precision LCR Meter was used. The C-V measurements were conducted under dark conditions and at 1 kHz frequency. The experimental setup can be seen in Figure 3.10.

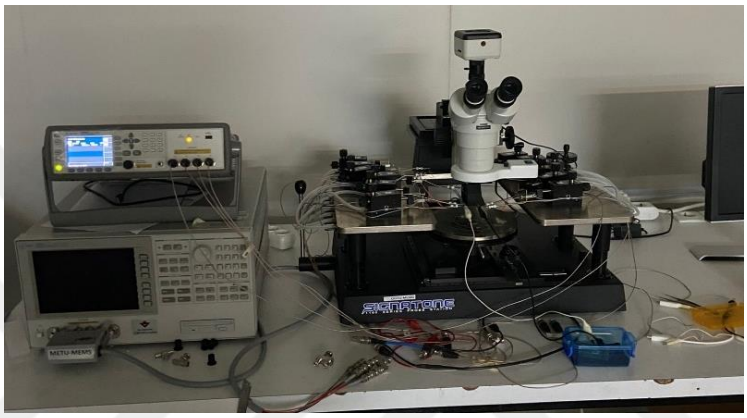

Figure 3.10. C-V measurement setup.

From C-V measurement Mott-Schottky analysis has been made by using the following equation[52]:

$$\frac{1}{C^2} = \frac{2\,(V_{bi} - V)}{A^2 q \varepsilon_0 \varepsilon_{PbS\,CQD} N_{PbS\,CQD}}$$

Where V_{bi} represents built-in voltage, V is applied voltage, A is area of the pixel, q is the electron charge, ε_0 is the permittivity of free space $\varepsilon_{PbS\,CQD}$ is the dielectric constant of PbS CQD, $N_{PbS\,CQD}$ is the carrier density of PbS CQD. V_{bi} values have been calculated by fitting the linear region of $1/C^2 \sim V$ curve. Then depletion width of the device has been calculated by using the following equation[52]:

$$W = \frac{1}{N_{PbS\ CQD}} \left[\frac{2\varepsilon_0 \varepsilon_{PbS\ CQD}(V_{bi} - V)}{q\left(\frac{1}{N_{PbS\ CQD}} + \frac{1}{N_{ZnO}}\right)} \right]^{\frac{1}{2}}$$

Where W represents depletion width and N_{ZnO} represents the carrier density of ZnO layer.

CHAPTER 4

RESULTS AND DISCUSSION

4.1 Characterization of the PTLE and DS PbS CQD Inks

To construct a well performing photodiodes and investigating the effect of PbS CQD inks derived from DS and PTLE methods on device performance, the PbS CQD and PbS CQD inks were thoroughly characterized. Firstly, the PbS CQDs were synthesized by conventional hot injection method and PbS CQD ink was obtained via PTLE method. The absorption spectrum of the oleate capped PbS CQDs (PbS-OA) in solution and TEM image of the PbS CQDs are represented in Figure 4.1-a and Figure 4.1-b, respectively.

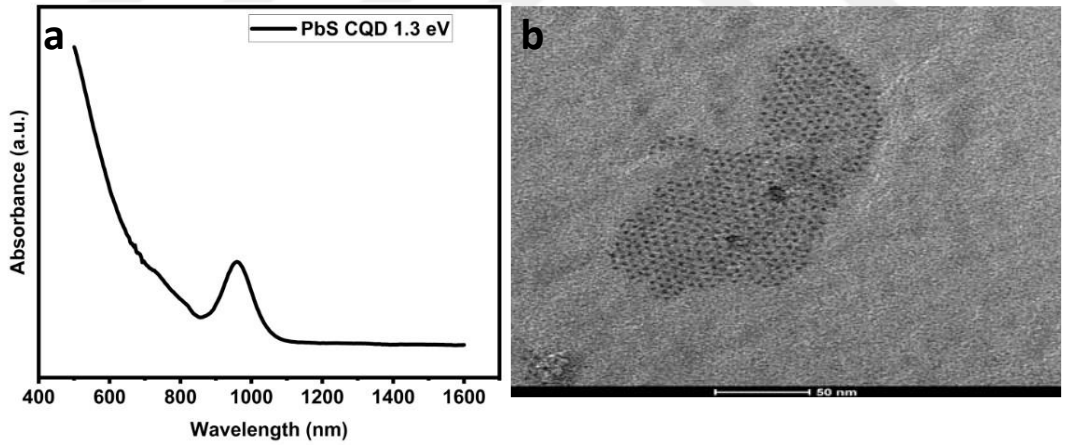

Figure 4.1. **a)** Absorbance of 1.3 eV PbS-OA CQD. **b)** TEM image of PbS CQD.

As represeneted in Figure 4.1-a, peak wavelength (λ_{max}) of the PbS QDs was determined as 960 nm and full width at half maximum (FWHM) was calculated as 100 nm. Moreover, size statsitics were studied on the TEM image represented in

Figure 4.1-b. According to the size statistics study (ImageJ software), the most frequent particle size occurred at 2.9 nm diameter.

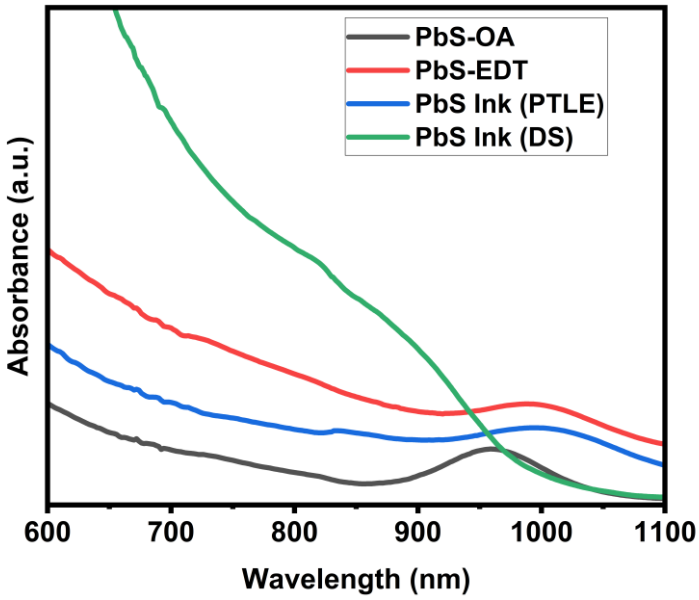

Figure 4.2. Absorbance of the thin film PbS-OA, EDT ligand exchanged (L-B-L) PbS CQD, PbS CQD ink derived from PTLE method and PbS CQD ink synthesized via DS method.

Figure 4.2 compares the absorbance of the PbS CQD inks that were prepared by PTLE and DS methods. PbS CQD inks prepared from PTLE method has λ_{max} at 994 nm with 430 nm FWHM. Widening of the excitonic peak, that is FWHM, was attributed to the ligand exchange process. It was reported that when exchanging ligands with halides, the initial excitonic peak tends to move towards longer wavelengths and becomes wider.[53] The variation in peak energies (OA < I) was explained by the loss of quantum confinement and the overlapping of electronic wave functions among individual CQDs in the film, which depends on the type of ligands.[53] In DS method, on the other hand, PbI_2 ratio in PbS CQD ink is higher compared to PTLE PbS CQD ink. Thus, in line with previous studies, the DS PbS ink showed a hypsochromic shift with an excitonic peak having an absorbance edge at ~920 nm (see Figure 4.2) .[22,23,27] To further investigate if the ligand exchange is

successful or not, FTIR analysis was conducted. Figure 4.3 shows the FTIR spectra of PbS-OA, PTLE PbS CQD ink, and DS PbS CQD ink.

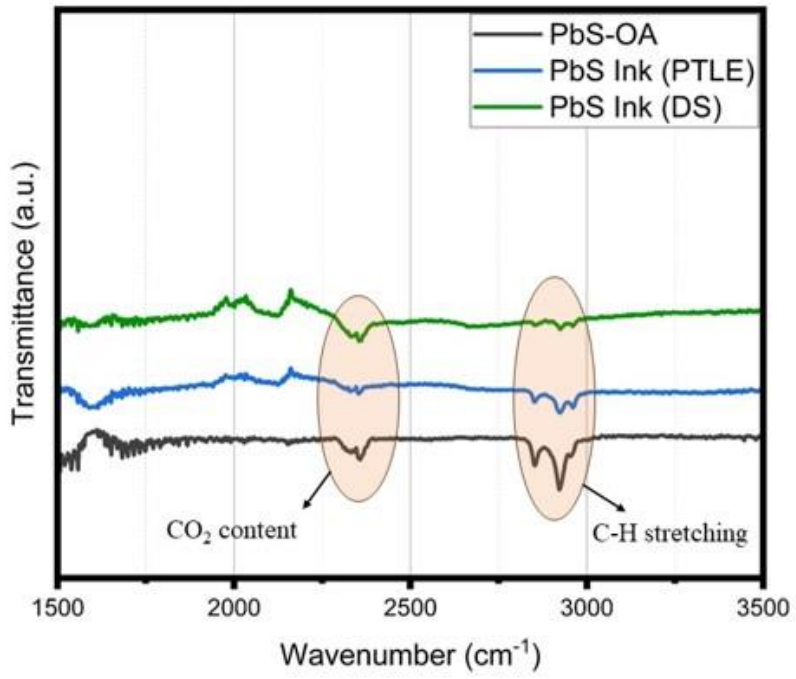

Figure 4.3. FTIR spectra of PbS-OA, PTLE PbS CQD ink, and DS PbS CQD ink.

According to Figure 4.3, the primary IR feature located at approximately 2900 cm^{-1} in the spectra of PbS-OA was attributed to the peaks corresponding to the stretching vibrations of CH bonds; asymmetric, CH_2 peaks at 2930 cm^{-1} and symmetric peaks at 2860 cm^{-1}. The reduction in these peaks for the PTLE PbS CQD ink indicates that the OA is efficiently removed.[54] For DS PbS ink, only a small peak was observed for the C-H stretching which was attributed to the DMF.[55] The peaks around wavenumber at 2350 cm^{-1} arise due to the small vibrations of CO_2 content in the infrared spectrometer during the experiments.[54]

4.2 SCAPS Simulation Results for the Device Architecture

Previous reports showed that the direction of the incident light affects the device performance.[40] To investigate whether illumination direction demonstrates a significant effect in SCAPS environment, I simulated the top illuminated (light strikes from ZnO side) and bottom illuminated (light strikes from PbS-EDT side) structures and compared their performance paramateres in terms of I-V, and EQE. The layer parameters for the simulations are represented in Table 3.1. The absorption spectrum data was integrated into the SCAPS for each layer in the device. The required absorption spectrums were obtained after the syntheses.

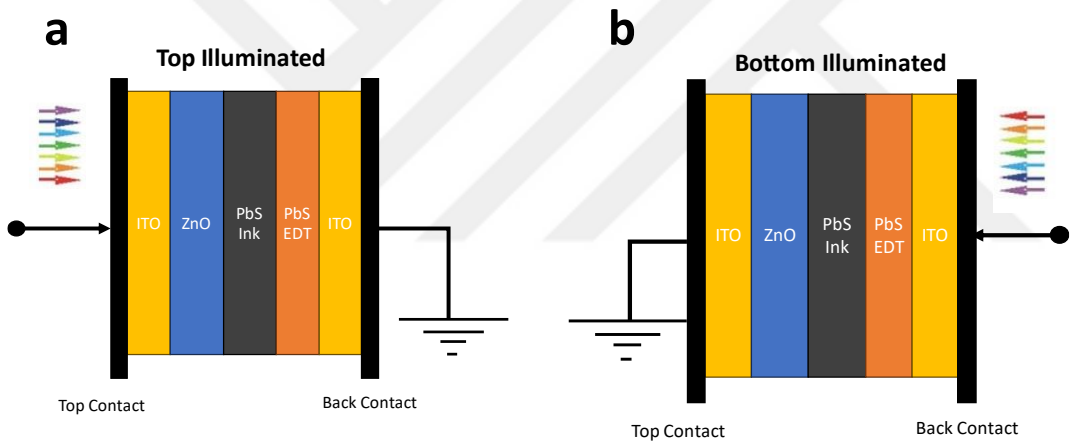

Figure 4.4. Device structure of PbS CQD photodiode for SCAPS **a)** top illuminated **b)** bottom illuminated.

Figure 4.4 shows the simulated device architectures for top and bottom illuminated devices. The top illuminated version of the device, where light strikes from the ZnO side and bottom illuminated device where light strikes from the PbS-EDT side are represented as in Figure 4.4-a and Figure 4.4-b, respectively.

To investigate whether the direction of the incident light has an effect on the current-voltage behavior, I simulated the IV, and EQE plot of both versions. Figure 4.5-a

shows the I-V performance of both cases. I found that top illumination offers slightly better performance in terms of I-V behavior which is in line with previously reported study.[40]

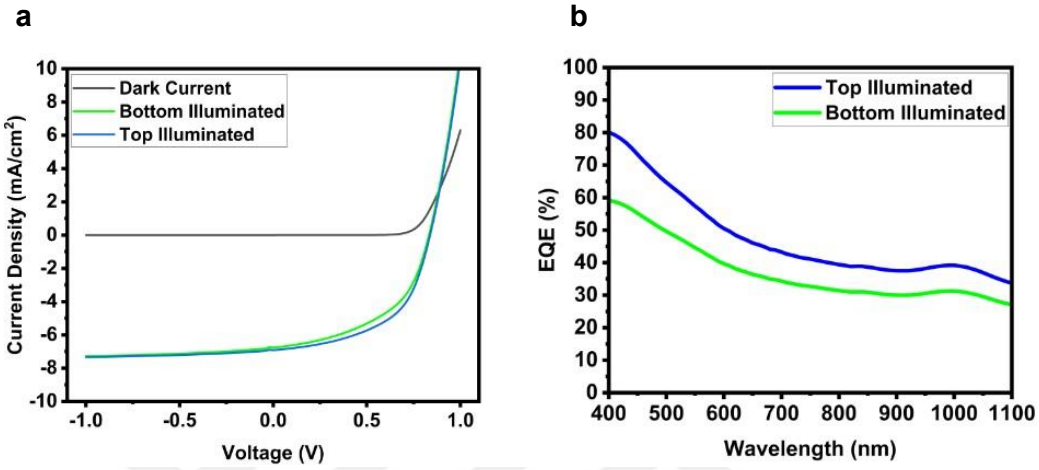

Figure 4.5. SCAPS **a)** I-V and **b)** EQE performance of PbS CQD photodiode for top and bottom illuminations.

The top illuminated device has 7.30 $mA.cm^{-2}$ current density whereas bottom illuminated device has 7.12 $mA.cm^{-2}$ at -0.5V. The dark current density of the device is 2.15 x 10^{-7} $mA.cm^{-2}$ at -0.5V for both cases.

Another important device parameter is the EQE. As Figure 4.5-b represents, the top illumination offers better quantum efficiency compared to the bottom illumination. For instance, top illuminated device exhibits ~40% EQE at 980 nm whereas the bottom illuminated EQE is ~31% at 980 nm. Based on the SCAPS simulations, we attributed the differences between the top and bottom illuminated devices to the absorption spectrum of the layers. Since PbS EDT layer has higher absorbance in IR portion of the electromagnetic spectrum, in the bottom illuminated structure, it prevents incident IR light from reaching the active layer. Thus, the lesser light reaches the PbS Ink layer. Since the electron-hole pairs are generated in the depletion region, lower electron-hole pairs are generated in the bottom illuminated case.

Therefore, as a result, the device architecture was determined to be ITO/ZnO/PbS Ink/PbS-EDT/Au architecture since the top illuminated structure gave better performance in terms of I-V characteristics and EQE during SCAPS simulations.

4.3 Comparison of PTLE & DS PbS Ink Devices

The DS PbS ink has several advantages as discussed in previous sections. Photodiodes with the device architecture ITO/ZnO/PbS Ink/PbS-EDT/Au were fabricated to compare the PTLE method with DS PbS ink, and for these devices, current-voltage, EQE, and response time measurements were made. Subsequently, specific detectivity values were calculated, and a detailed comparison was made.

4.3.1 Current-Voltage Measurement Results

The main aim of this characterization was determining the dark current which dominates the noise current. The measurements were conducted under 980 nm light to see the photodiode behavior of the device under light conditions. In addition, the dark current was also measured for the detectivity calculations.The active device area was 0.045 cm^2 which was used to calculate the dark current densities. The I-V graph for the photodiodes with DS and PTLE PbS Inks are indicated in Figure 4.6-a and Figure 4.6-b, respectively.

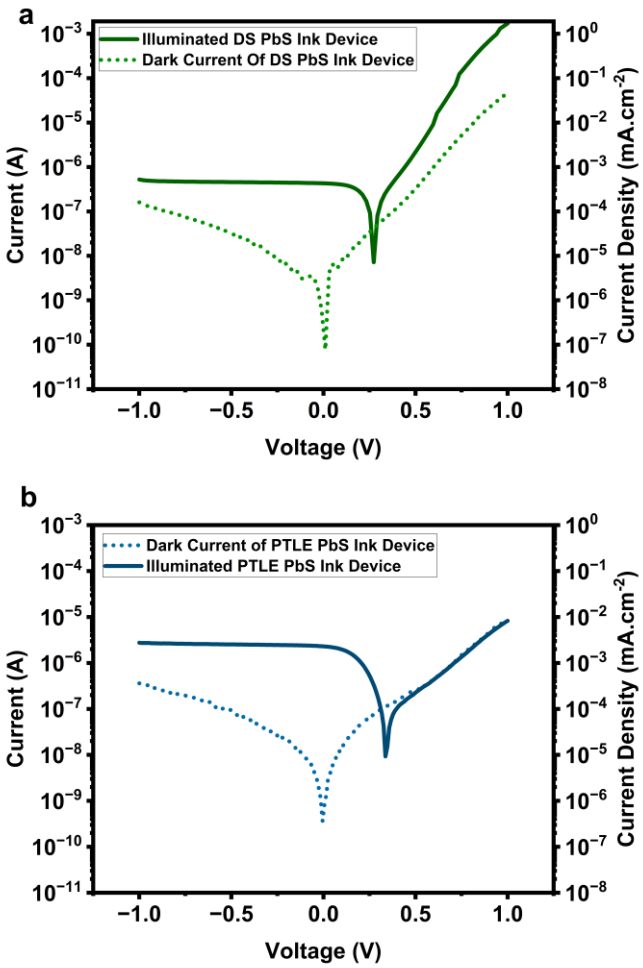

Figure 4.6. I-V results for photodiode devices with **a)** DS PbS Ink and **b)** PTLE PbS Ink.

The photodiode that contains DS PbS Ink in Figure 4.6-a, has 3.42 x 10^{-8} A dark current under -0.5 V bias and 1.03 x 10^{-10} A dark current at 0 V bias. That means the device has 7.6 x 10^{-4} mA.cm^{-2} dark current density at -0.5 V bias and 2.28 x 10^{-6} mA.cm^{-2} at 0 V bias. The photodiode that contains PTLE PbS Ink in Figure 4.6-b, has 1.96 x 10^{-7} A dark current under -0.5 V bias and 9.25 x 10^{-8}A at 0 V bias. That means the device has 4.36 x 10^{-3} mA.cm^{-2} dark current density at -0.5 V and 2.1 x 10^{-3} mA.cm^{-2} at 0 V bias. As a result, I found that the DS PbS inks has lower dark current density as compared to PTLE PbS inks.

4.3.2 EQE, Spectral Response and Specific Detectivity Results

EQE measurements were conducted at -0.5V reverse bias for both photodiodes where one of them contains DS PbS Ink and the other one contains PTLE PbS Ink. The EQE results for the devices are shown in Figure 4.7.

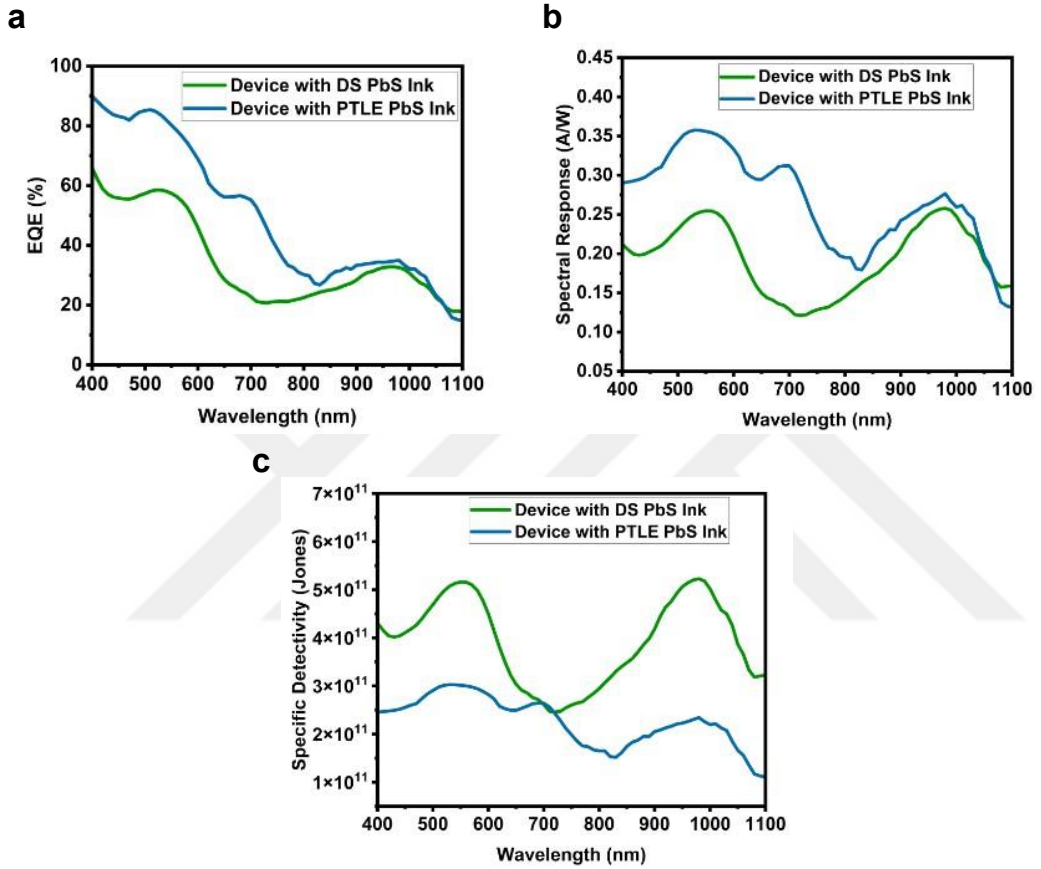

Figure 4.7. **a)** EQE, **b)** spectral response, and **c)** specific detectivity results for both device with DS PbS Ink and PTLE PbS Ink.

According to Figure 4.7-a, the device with PTLE PbS Ink has 35.02 % EQE at 980 nm whereas the DS PbS Ink shows 32.64 % EQE at 980 nm wavelength. Moreover, according to Figure 4.7-b, photodiode device with PTLE PbS Ink offers higher spectral response values at all wavelengths. At 980 nm, the photodiode with PTLE PbS Ink shows 0.28 A/W spectral responsivity whereas the photodiode with DS PbS Ink shows 0.25 A/W spectral responsivity. Specific Detectivity (D^*) is an important

figure of merits for the photodiodes. Thus, D^* was calculated for both devices by using the equations that are provided in section 2.5.2 and the obtained spectra are represented in Figure 4.7-c. According to Figure 4.7-c., the photodiodes with DS PbS Ink has 5.23 x 10^{11} Jones specific detectivity whereas the photodiode device with PTLE PbS Ink has 2.34 x 10^{11} Jones specific detectivity at 980 nm (under -0.5 V reverse bias). The higher specific detectivity of the DS PbS inks was attributed mainly to the their relatively lower dark currents.

4.3.3 Rise & Fall Time Measurement Results

The rise and fall time measurements were conducted for both photodiodes with DS and PTLE Inks. The rise time and fall time measurement results for the photodiode with DS PbS Ink are shown in Figure 4.8-a. A closer look of the signal that was obtained via oscilloscope for the DS PbS Ink device is represented in Figure 4.8-b and Figure 4.8-c.

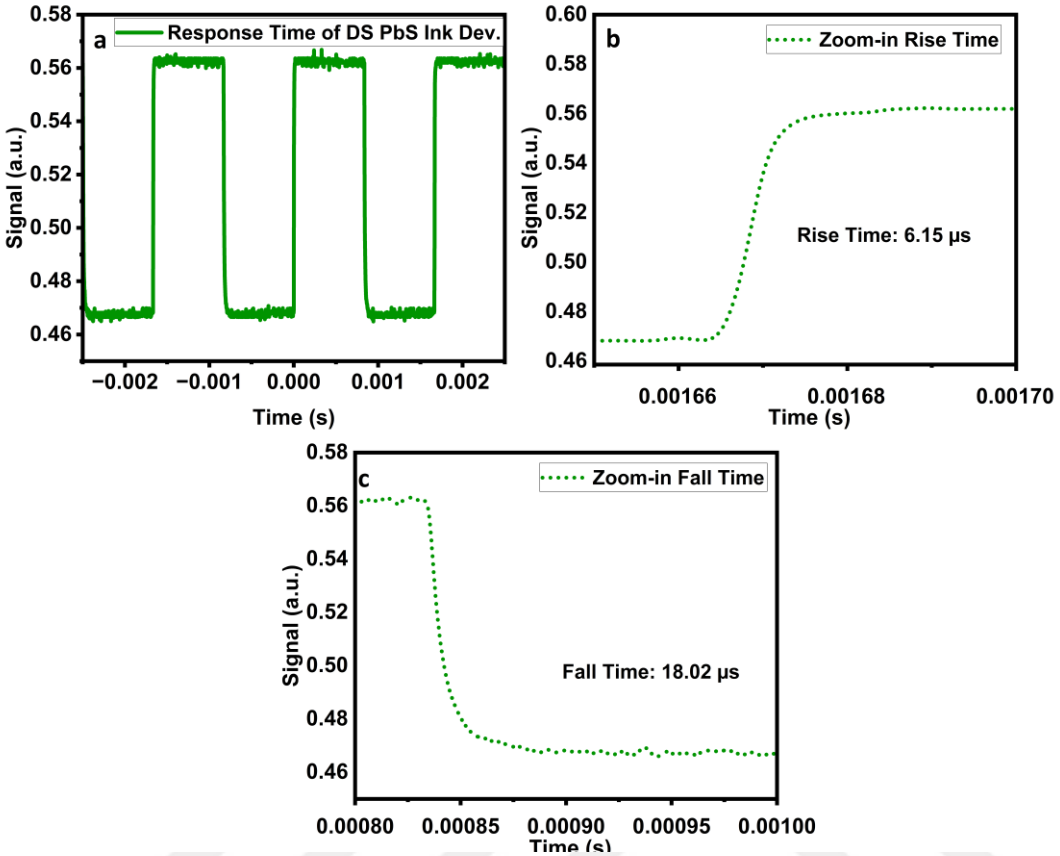

Figure 4.8. **a)** The rise/fall time signals in a larger scale, **b)** closer look to the rise time, **c)** closer look to the fall time signals for devices with DS PbS Ink.

According to the Figure 4.8-b, rising edge indicates that required time for a pulse to rise from 10% to 90% is 6.15 µs whereas falling edge, Figure 4.8-c, indicates that required time for a pulse to fall from 90% to 10% is 18.02 µs for the photodiodes with DS PbS Ink.

I found that the rise / fall time values for PTLE PbS inks are different from the photodiodes with DS PbS Ink. The obtained signals are represented in Figure 4.9-a Figure 4.9-b and Figure 4.9-c.

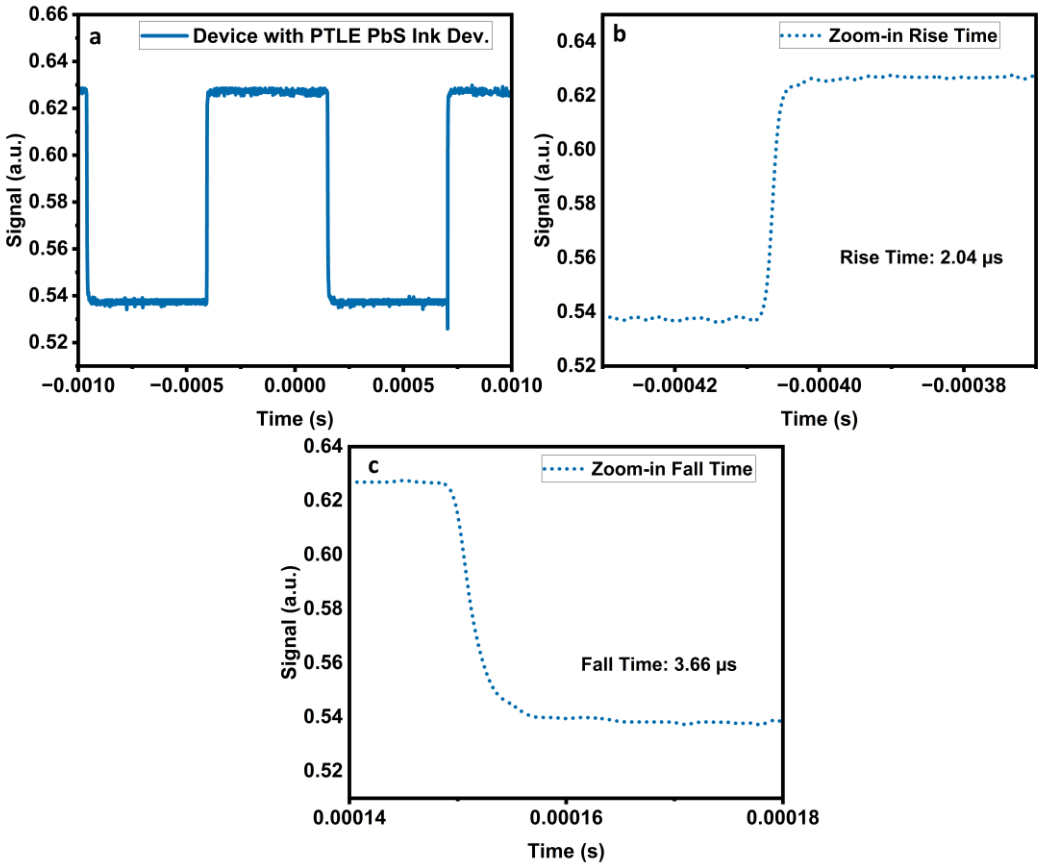

Figure 4.9. **a)** The rise/fall time signals in a larger scale, **b)** closer look to the rise time, **c)** closer look to the fall time signals for devices with PTLE PbS Ink.

According to the Figure 4.9-b, rising edge indicates that required time for a pulse to rise from 10% to 90% is 2.04 µs whereas, Figure 4.9-c, falling edge indicates that required time for a pulse to fall from 90% to 10% is 3.66 µs for the photodiodes with PTLE PbS Ink.

As a result, I found that the DS PbS inks, although they have relatively higher specific detectivity due to their low dark current density slightly higher rise/fall time compared to PTLE PbS inks.

4.3.4 Overall Comparison

In this section, the produced photodiode structures with DS PbS Ink and PTLE PbS Ink are compared. The notation for samples is explained in Figure 4.10-a and order of the pixels within a device is shared in Figure 4.10-b.

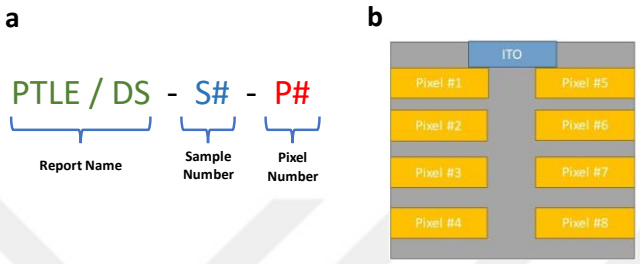

Figure 4.10. **a)** Experimental notations for this study. **b)** Representation of the pixel orders.

Within the scope this study, various photodiodes containing DS PbS Ink and PTLE PbS Ink as active materials were produced. The results of champion devices are summarized in Table 4.1. All parameters except rise/fall time in Table 4.1 are collected under -0.5V bias. Rise / fall time values are collected when the photodiode is at self-powered state. Errors for each sample are estimated by measuring different pixels on the same device. The achieved EQE values for both photodiodes were close to each other. However, photodiode with DS PbS Ink has lower dark current density. Consequently, the photodiode with DS PbS Ink possess higher detectivity compared to the photodiode with PTLE PbS Ink. On the other hand, both rise and fall time values are high for the DS PbS Ink photodiode whereas the PTLE PbS Ink photodiode has lower. This means that the PTLE PbS Ink photodiode offers a higher speed in terms of light detection.

Table 4.1 Comparison of the photodiodes that are produced within this study.

Architecture of the Produced Photodiodes	*J_D @ -0.5V (mA.cm^{-2})*	*EQE*	*D^* (Jones)*	*Rise / Fall Time (μs)*	*Code of the Experiment*
ITO/ZnO/DS PbS Ink/PbS-EDT/Au	7.6 ± 0.29 x 10^{-4}	32.64 ± 1.8% @ *980 nm*	5.23 ± 0.6 x 10^{11}@ *980 nm*	6.15 ± 2.1 / 18.02 ± 1.8	DS-S1-P5
ITO /ZnO/PTLE PbS Ink/ PbS-EDT/Au	4.36 ± 0.38 x 10^{-3}	35.02 ± 2.4% @ *980 nm*	2.34 ± 0.81 x 10^{11}@ *980 nm*	2.04 ± 0.58 / 3.66 ± 0.15	PTLE-S1-P7
ITO /ZnO/DS PbS R1/ PbS-EDT/Au	1.94 x 10^{-5}	23.4 @ *920 nm*	1.83 x 10^{12} @920nm	21.12/76.33	DS(R1)-S1-P3
ITO /ZnO/DS PbS R2 (optimized)/ PbS-EDT/Au	1.96 x 10^{-8}	35.19 @ *920 nm*	**1.5 x 10^{13}** @920nm	**1.65/8.08**	DS(R2)-S3-P6

4.4 Further Optimization of DS PbS CQD Based Photodiodes

Due to their lower dark current densities, DS PbS inks have a greater potential to achieve higher detector performance parameters and therefore we carried out further optimization studies. Currently, it is only synthesized in the literature with a specific recipe due to being a new method as explained in section 2.4.3. The main disadvantage of the DS PbS inks is its poorer monodispersity as compared to conventional PTLE inks, which causes an absorption edge rather than a distinct absorption peak. Therefore, it is necessary to explore the kinetics of the DS PbS ink synthesis method and modify the QD nucleation and growth stages.

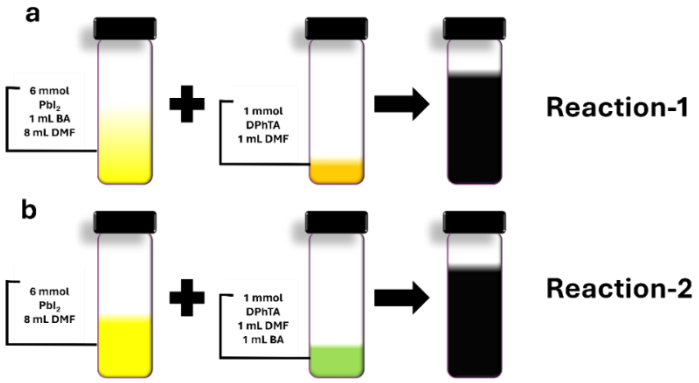

Figure 4.11. Representation of **a)** Reaction-1 and **b)** Reaction-2.

In the literature, kinetic studies of DS PbS ink are typically conducted by first dissolving the sulfur precursor, DPhTA, in DMF, and then injecting it into a solution containing PbI_2 as illustrated Figure 4.11-a which is called as Reaction-1 (R1).[27] However, in these studies, the sulfur precursor DPhTA, after forming -SH groups, takes time to find Pb ions and form quantum dots, prolonging the synthesis process and reducing monodispersity. Therefore, in this part of the study, DPhTA was pre-dissolved in butylamine to form -SH groups before injection, and then added to DMF and PbI_2 solution as showed in Figure 4.11-b which was called as Reaction-2 (R2).

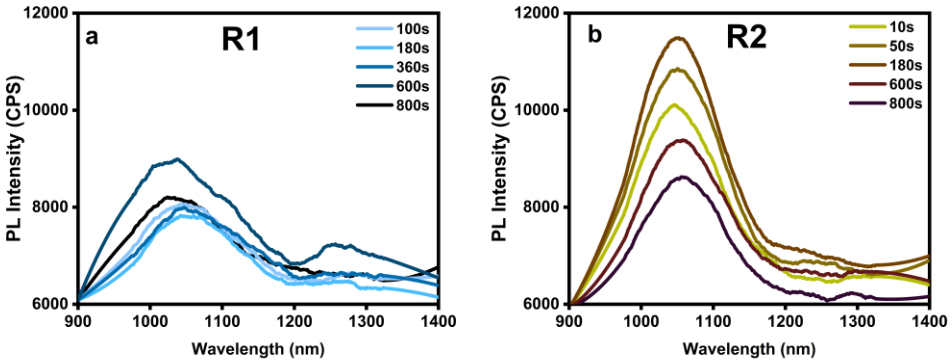

Figure 4.12. Normalized PL intensity comparison for **a)** R1 ink and **b)** R2 ink.

Figure 4.12 represents the PL intensities of the normalized DS PbS inks. Due to its low stability, at 10 and 50 seconds, we couldn't observe any meaningful PL intensity for the R1. Moreover, as it can be seen in Figure 4.12 -a, for the R1, the maximum

PL intensity was achieved for 600 seconds. Additionaly, at ~1300nm, the defects were observed for the R1 when the duration was set as 800 seconds. On the other hand, the maximum PL intensity was achieved at 180 seconds for the R2 ink as in Figure 4.12-b, and no significant defects were observed for the R2. Thus, the formation of PbS quantum dots was accelerated via R2, and the reaction time was reduced from 10 minutes to 3 minutes.

Firstly, to compare the kinetics of reactions R1 and R2, separate experiments were conducted to plot the La Mer diagrams. Since both reactions could be quenched with toluene, 200 µL of toluene was filled into mini centrifuge tubes before initiating the reactions. After starting the reactions, at specific time intervals, DS PbS CQD ink solution was drawn into a syringe to reach 100 µL and swiftly transferred into the toluene solution.

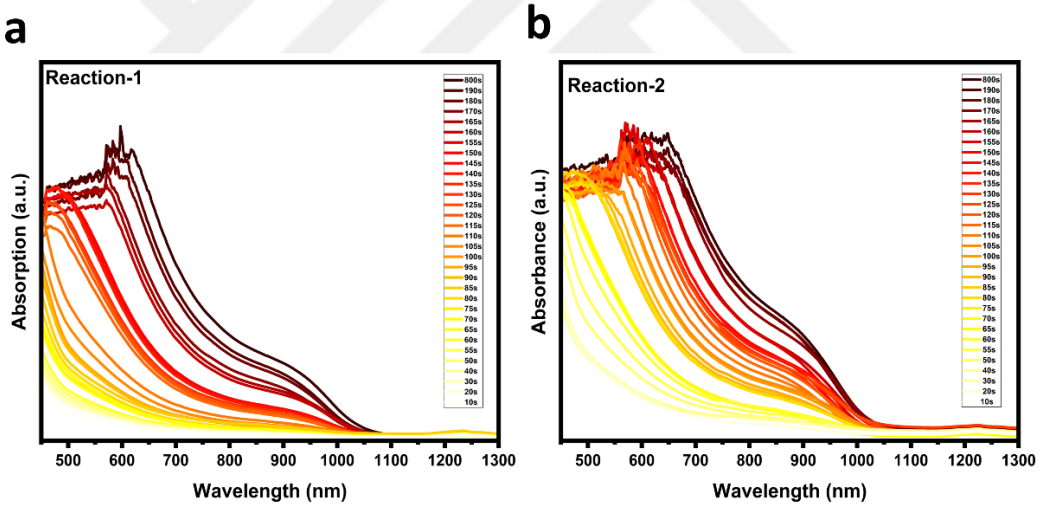

Figure 4.13. **a)** Absorption spectrum of R1 and **b)** absorption spectrum of R2 at different reaction times.

Figure 4.13-a shows the absorption spectrum of R1 for different times. It is observed that the synthesis of R1 possesses 3 major steps until the formation of final absorption edge. On the other hand, the synthesis of R2 continues uninterrupted until the final absorption edge is formed as depicted in Figure 4.13-b .

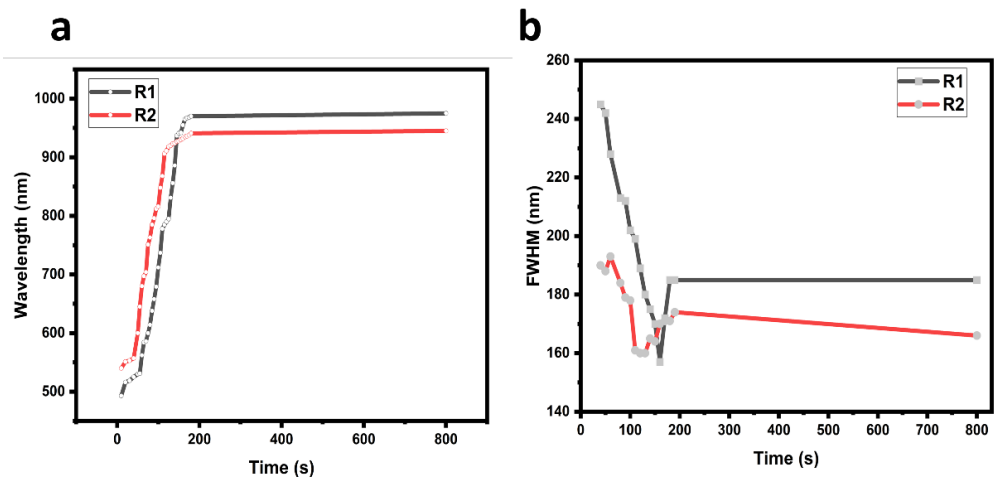

Figure 4.14. **a)** Band edge absorption as a function of time for R1 and R2.**b)** Change of FWHM with time for R1 and R2.

Based on these absorption spectrums, change of band edge absorption values was plotted as a function of time and the graph is represented in Figure 4.14-a. It indicates that the reaction in R2 occurs with a faster rate as compared to R1. For both cases the absorption edge was nearly observed at ~900nm. Moreover, the full width half maximum of the absorption edges was calculated to reveal the difference between R1 and R2 as shown in Figure 4.14-b. We found thatR2 has relatively lower FWHMs when compared to R1. This difference in FWHMs between R1 and R2 was attributed to the better size uniformity of R2.

Finally, I found that the yield of the reaction shows a strong dependence on the reaction kinetics. I noted that the R2 QD ink yield was 42% higher as compared to R1.

To see the real potential of R2, the same photodiode structures were reconstructed where the active materials were R1 and R2.

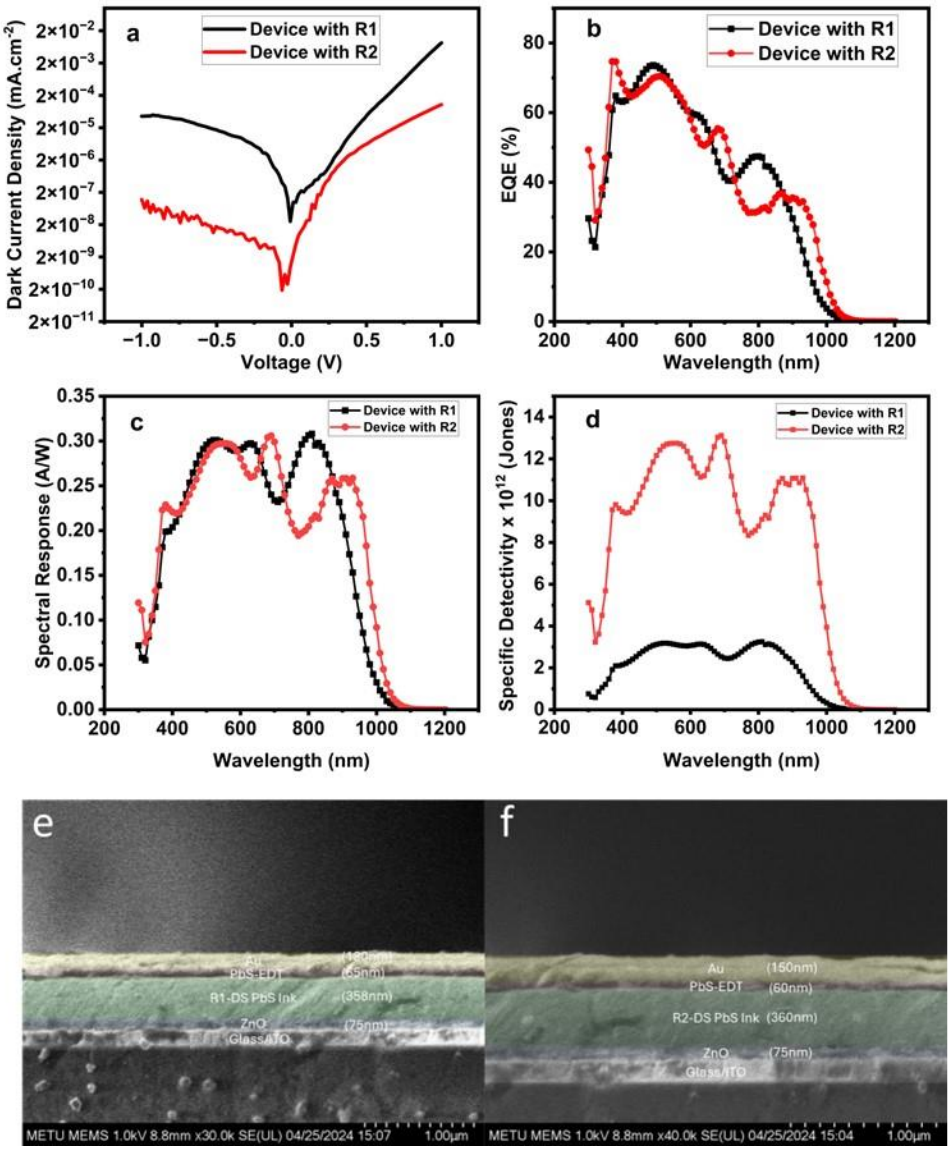

Figure 4.15. R1 and R2 device comparison in terms of **a)** dark current, **b)** EQE, **c)** spectral response, **d)** specific detectivity in ITO/ZnO/DS PbS Ink/PbS-EDT/Au architecture. Cross sectional SEM image of **e)** R1 device, **f)** R2 device.

The dark currents and EQE results are represented in Figure 4.15. According to Figure 4.15-a, device with R2 exhibits relatively lower dark current in the range of ~10^{-11}A under 0 bias voltage whereas the R1 device achieved ~10^{-9} A under 0 bias voltage. Notably lower dark current recorded for the R2 was attributed to the higher quality, that is monodispersity, of DS PbS inks (see Figure 4.14-b). In near infrared

region, however, R1 device showed higher EQE than R2 device as shown in Figure 4.15-b, Figure 4.15-c, respectively. Yet, in terms of specific detectivity R2 has better performance as shown in Figure 4.15-d. The likely reason for this is that R2 possesses notably lower dark currents as compared to R1 which can be assigned to the more uniform size distribution and lower defect density. As a result, while R1 device has a detectivity value in the range of 10^{12} Jones, the R2 device can reach up to 10^{13} Jones. To ensure that the thickness of the layers was the same for both types of devices, we carefully examined the SEM images. Figure 4.15.e and Figure 4.15-f show the cross-sectional SEM images of the photodiodes fabricated from R1 and R2. We found that the ZnO ETL and PbS-EDT layers were 75 nm and 60-65 nm for both devices. Additionally, the thicknesses of the R1 and R2 active layers were found to be 358 and 360 nm, respectively. Thus, we eliminated the effect of thickness on the device performance comparison.

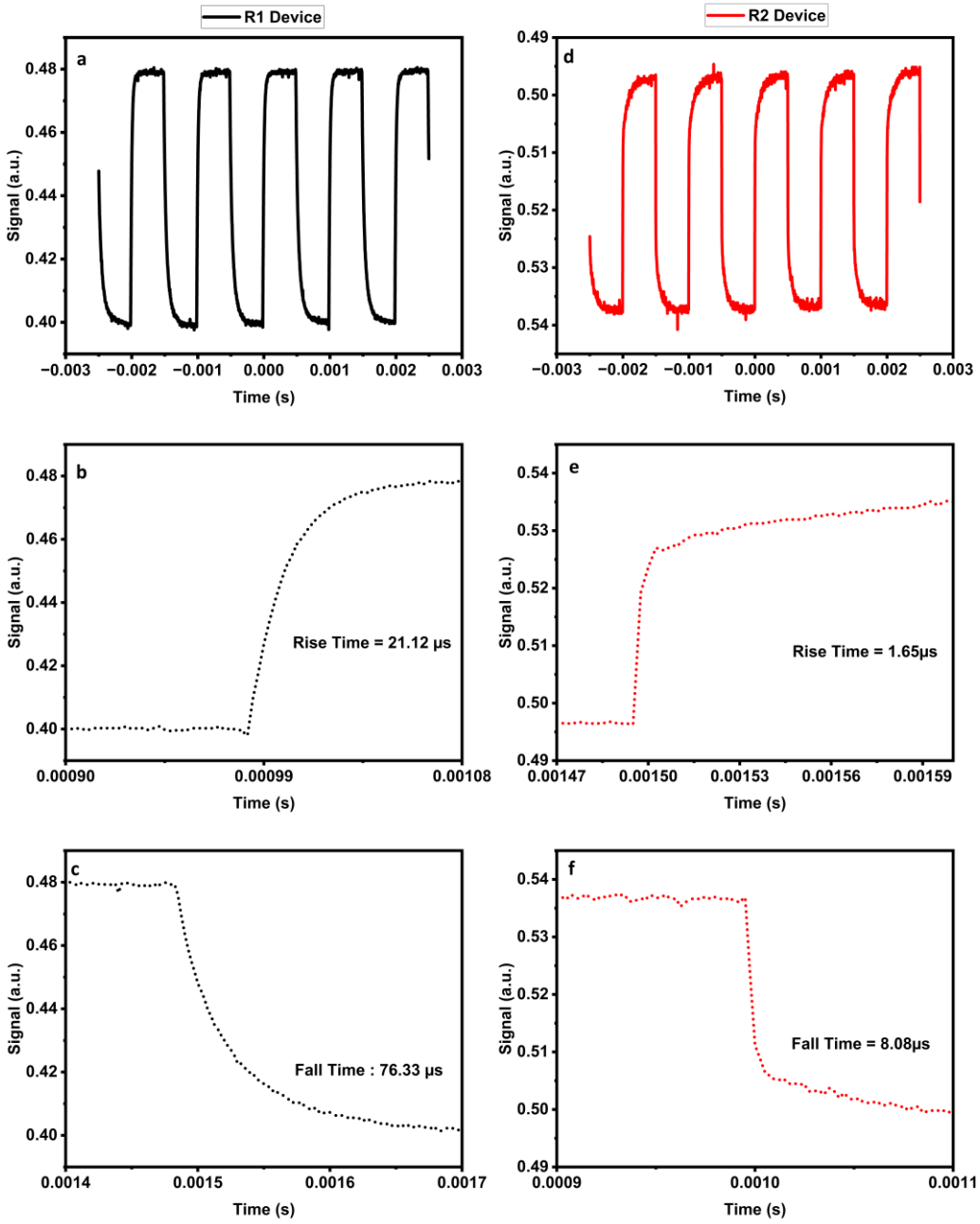

Figure 4.16. Response time of R1 where **a)** large scale, **b)** rise time, **c)** fall time and response time of R2 where **d)** large scale, **e)** rise time and **f)** fall time.

Subsequently, to examine the differences in response times, pulses at 1 kHz were sent from 920 nm LED light to measure the response times of R1 and R2 devices. We noted that the optimization of the synthesis method through control over size

distribution has a profound effect on the response times. Response time of R1 is indicated in Figure 4.16-a where its rise and fall times were recorded as 21.12 µs and 76.33 µs, respectively (see Figure 4.16-b and Figure 4.16-c). Response time of R2 device is represented in Figure 4.16-d where its rise and fall time were recorded as 1.65 µs and 8.08 µs, respectively. These significant differences in response times of R1 and R2 suggest a potential discrepancy in defects between R1 and R2 devices which was also verified by the PL experiments.

To have a better understanding of the effects of defects in DS PbS ink layer, we applied C-V measurements on ITO/ZnO/DS PbS Ink (R1 and R2)/PbS-EDT/Au devices under dark conditions.

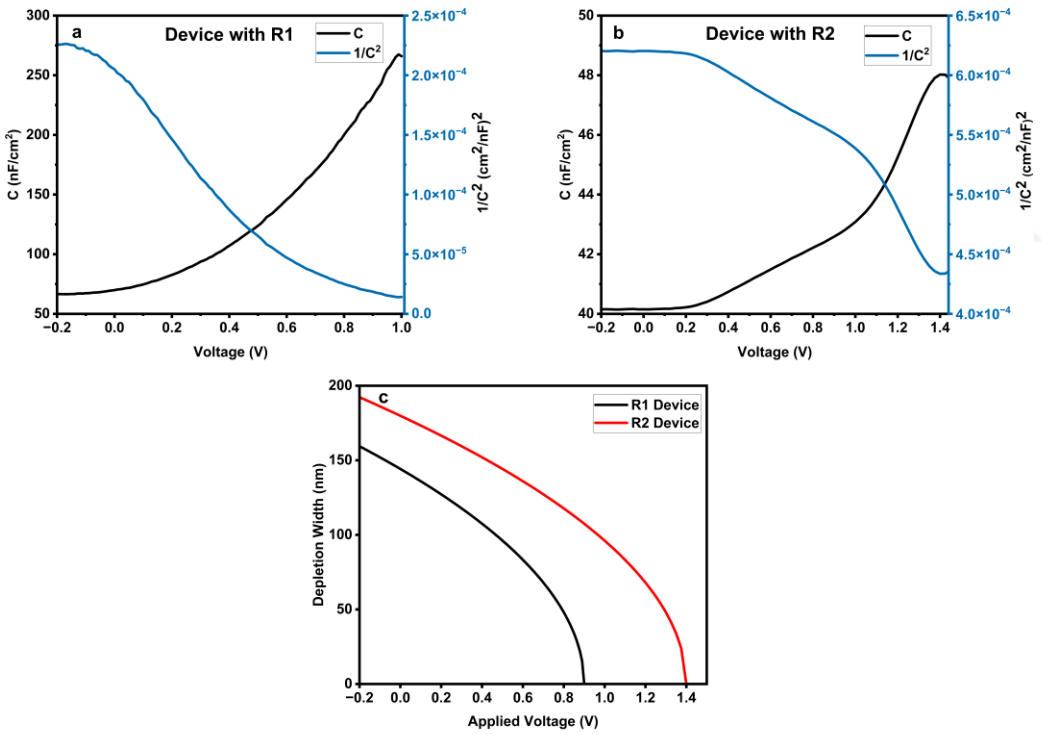

Figure 4.17. Capacitance-Voltage measurements and Mott-Schottky analysis for **a)** device with R1 and **b)** device with R2. **c)** calculated depletion width of ITO/ZnO/DS PbS Ink R1 or R2/ PbS-EDT/Au device.

Figure 4.17-a represents the C-V analysis for the R1 and R2 devices. For R1, V_{bi} was found as ~0.91 V whereas for R2 it was in the range of~1.4 V (see Figure 4.17-b). Higher V_{bi} of R2 suggests that the device with R2 facilitates a higher charge carrier extraction when compared to R1 device.[52] Moreover, Figure 4.17-c represents the effect of R1 and R2 on the depletion width. According to our calculations from Mott-Schottky analysis, the depletion width of R2 was notably larger than R1 device. Wider depletion widths observed in R2 devices suggests a higher electron-hole pair generation rate for R2. This might lead to a more efficient photon collection and consequently, higher detectivities.

4.5 The Future Potential of DS PbS Ink Through SCAPS

The DS PbS ink showed a remarkable performance in terms of detectivity. Yet, it might be far more efficient to choose a better ETL and HTL combination. Thus, in this part of the thesis, for the first time in literature systematic simulations were conducted to find the best device architecture for the DS PbS ink. The SCAPS parameters for the DS PbS ink, HTLs and ETLs were extracted from the previous reported studies. Moreover, the absorption spectrum of the ETL and HTL layer was calculated via SCAPS default settings whereas for the DS PbS ink layer, obtained absorption spectrum within this study was used.

To determine the best HTL and ETL combination, various ETLs and HTLs having different band alignments were utilized. Several HTLs such as PbS-EDT, poly(ethylene-3,4-dioxythiophene):poly(styrenesulfonic acid) (PEDOT:PSS), copper (I) iodide (CuI), copper (I) oxide (CuO), copper (II) oxide (Cu_2O), copper(I) thiocyanate (CuSCN), molybdenum trioxide (MoO_3), nickel oxide (NiO) and 2,2′,7,7′-Tetrakis[N,N-di(4-methoxyphenyl)amino]-9,9′-spirobifuorene (Spiro-MeOTAD) were used. On the other hand, various types of widely used ETLs such as ZnO, titanium dioxide (TiO_2), tin (IV) oxide (SnO_2), indium gallium zinc oxide (IGZO), fullerene (C_{60}), cadmium sulfide (CdS) and cerium (IV) oxide (Ce_2O) were utilized. To achieve realistic simulation and analysis of the semiconductor devices,

it is essential to integrate accurate and reliable optoelectronic properties for all the materials employed in the simulation.

SCAPS parameters used for the DS PbS Ink and other HTL materials are represented in Table 4.2. The thickness of HTLs were set at 50 nm and thickness of the DS PbS ink layer was considered to be 300 nm. Moreover, the SCAPS parameters for the ETLs can be seen in Table 4.3. For the ETLs, the thickness was considered as 100 nm. For both HTLs and ETLs, the electron and hole thermal velocity was set as 10^7 cm/s as given in the references for the materials.

Table 4.2. The basic SCAPS parameters for DS PbS Ink and HTLs.

Parameters	**Active Material**	**Hole Transport Layers**								
	DS PbS Ink	**PbS-EDT**	**PEDOT:PSS**[56,57]	**CuI**[56,58]	**CuO**[5,6,59]	**Cu_2O**[5,6,60–62]	**CuSCN**[56,60]	**MoO_3**[63–65]	**NiO**[56,66,67]	**Spiro-MeOTAD**[48,56]
Thickness (nm)	300 (Varied)	50	50	50	50	50	50	50	50	50
Bandgap (eV)	1.4	1.4	1.6	3.1	1.51	2.17	3.6	3	3.6	3
Electron affinity (eV)	4	3.5	3.4	2.1	4.07	3.2	1.7	2.5	1.8	2.2
Dielectric permittivity	19.8	20	3	6.5	18.1	7.1	10	12.5	11.7	3
CB effective density (10^{19} cm^{-3})	1	1	0.22	2.8	2.2	0.02	2.2	0.22	25	0.22
VB effective density (10^{19} cm^{-3})	1	1	1.8	1	55	1.1	0.18	1.8	25	1.8
Electron mobility ($cm^2/V{\cdot}s$)	0.0267	$2x10^{-4}$	$4.5x10^{-2}$	100	100	200	100	25	2.8	$2.1x10^{-3}$
Hole mobility ($cm^2/V{\cdot}s$)	0.0267	20	$4.5x10^{-2}$	43.9	0.1	80	25	100	2.8	$2.16x10^{-3}$
Shallow uniform donor density ND (cm^{-3})	$8.77x10^{16}$ (Varied)	10^{14}	0	0	0	0	0	0	0	0
Shallow uniform acceptor density NA (cm^{-3})	0 (Varied)	10^{16}	10^{18}	10^{18}	10^{18}	10^{18}	10^{18}	10^{18}	$3x10^{18}$	10^{18}
Defect Density (cm^{-3})	10^{14} (Varied)	10^{15}	10^{15}	10^{15}	10^{15}	10^{15}	10^{15}	10^{15}	10^{15}	10^{15}

Table 4.3. The basic SCAPS parameters for DS PbS Ink and HTLs.

Parameters	**Electron Transport Layers**						
	ZnO[56,68]	**TiO_2**[56,69]	**SnO_2**[70]	**IGZO**[56]	**C_{60}**[56,71]	**CdS**[68,72]	**CeO_2**[56]
Thickness (nm)	100	100	100	100	100	100	100
Bandgap (eV)	3.3	3.2	3.6	3.05	1.7	2.4	3.5
Electron affinity (eV)	4.2	4.26	4.5	4.16	4.5	4.5	4.6
Dielectric permittivity	9	9	9	10	6	10	9
CB effective density (cm^{-3})	$3.7x10^{18}$	$2.2x10^{18}$	$2.2x10^{18}$	$5x10^{18}$	10^{19}	$1.5x10^{18}$	10^{20}
VB effective density (cm^{-3})	$1.8x10^{19}$	$1.8x10^{19}$	$1.8x10^{19}$	$5x10^{18}$	10^{19}	$1.8x10^{18}$	$2x10^{21}$
Electron mobility ($cm^2/V{\cdot}s$)	100	20	100	15	50	50	100
Hole mobility ($cm^2/V{\cdot}s$)	25	10	25	0.1	50	20	25
Shallow uniform donor density ND (cm^{-3})	10^{18}	10^{19}	10^{20}	10^{17}	10^{18}	10^{17}	10^{21}
Shallow uniform acceptor density NA (cm^{-3})	0	0	0	0	0	0	0
Defect Density (cm^{-3})	10^{15}	10^{15}	10^{15}	10^{15}	10^{15}	10^{15}	10^{15}

The most experimentally successful conventional device architectures reported so far has ITO/ZnO/DS PbS Ink/PbS-EDT/Au device structure where DS PbS Ink acts as the main absorber layer, ZnO as the ETL, and PbS-EDT acts as the HTL. Based on a recent study reported by Wang et al., this device structure achieved a very promising solar cell photoconversion efficiency (PCE) in the range of 12.12% PCE.[22] To verify the SCAPS parameters (Table 4.2 and Table 4.3) I used throughout my study, this device architecture was chosen as a control cell.

Table 4.4. Comparison of the simulated and reported ITO/ZnO/DS PbS ink/PbS-EDT/Au cell.

	Voc (V)	**Jsc ($mAcm^{-2}$)**	**FF (%)**	**PCE (%)**	**Year**
Previous Report	0.63	25.1	64.0	10.1	(2019)[23]
Simulated	0.81	23.1	58.5	10.9	(2024) This Thesis

As summarized in Table 4.4 , cell parameters simulated within SCAPS environment were compared with the previous report. The fact that we reached cell parameters that are very close to the previously reported control cell indicates the validity of the SCAPS parameters. Previous studies reported that the mobile ions cause hysteresis and photo instability in quantum dot solar cells.[73] Therefore, the negligibly small differences between the experimental and simulation results might be attributed to the mobile ions which cannot be simulated within SCAPS environment.[48,74]

4.5.1 ETL and HTL Combination Study

To determine the best ETL-HTL combination for DS PbS Ink based solar cells, 63 different device structures were simulated as shown in Figure 4.19 . Considering all the ETL-HTL combinations, the best device performances were achieved for MoO_3 as the HTL.

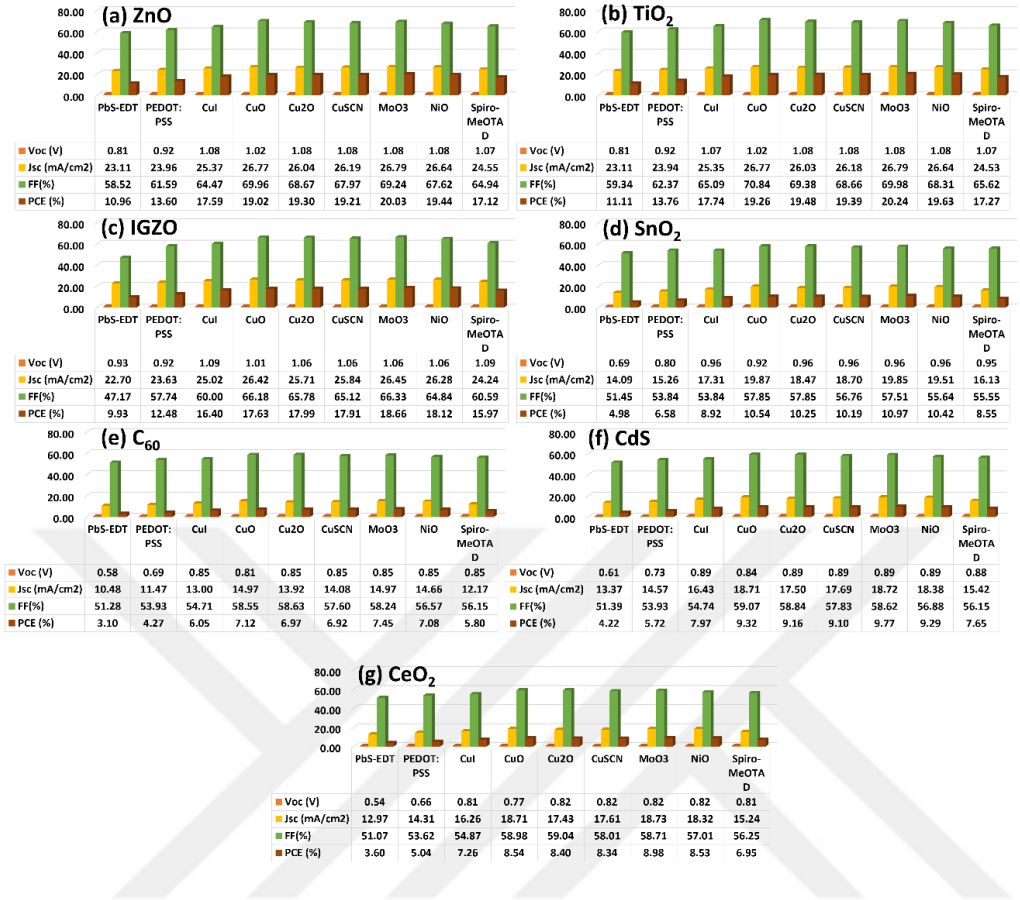

Figure 4.18. ETL (thickness = 100 nm) and HTL (thickness = 50 nm) combinations for DS PbS ink (thickness = 300 nm) based solar cells where the ETLs are: **(a)** ZnO, **(b)** TiO_2, **(c)** IGZO, **(d)** SnO_2, **(e)** C_{60}, **(f)** CdS, **(g)** CeO_2.

On the other hand, several ETL materials achieved remarkable efficiencies over 18%. Solar cells where ZnO (Figure 4.18-a.), TiO_2 (Figure 4.18-b) and IGZO (Figure 4.18-c)) used as the ETL and MoO_3 as the HTL achieved 20.03%, 20.24% and 18.66% PCE, respectively. Moreover, the combination of MoO_3 HTL with SnO_2 (Figure 4.18-d), C_{60} (Figure 4.18-e), CdS (Figure 4.18-f), and CeO_2 (Figure 4.18-g) ETLs achieved 10.97%, 7.45%, 9.77%, and 8.98% PCE, respectively. Consequently, the best device architecture was determined as ITO/TiO_2/DS PbS Ink/MoO_3/Au. This device architecture was used for further simulation studies in the next sections.

4.5.2 The Effect of Dopant Type

Liu et al. stated that adding bifunctional thiol molecules makes DS PbS Ink more n-type whereas addition of monofunctional thiol molecules makes DS PbS Ink more p-type.[49] According to the reported studies, the synthesized p-type PbS CQD inks achieved a higher PCE when compared to n-type inks.[75] Moreover, it has widely known that the PbS-QD based optoelectronic devices have not yet reached the desired performance due to the presence of defects induced during synthesis and/or solar cell fabrication steps.[76] Therefore, examining the sources of defects and their possible effects on cell performance and developing strategies to prevent these defects are the most effective tools to overcome this bottleneck. Thus, to explore the response of the cell against defects for both dopant types, DS PbS ink was simulated at various dopant concentrations over different defect densities. Figure 4.19 demonstrates the concurrent effects of dopant type/concentration and defect density on the cell parameters. The thickness of DS PbS ink layer was fixed at 300 nm during this simulation. The acceptor and donor concentration of DS PbS ink varied from 10^{13} to 10^{22} cm^{-3} whereas natural defect density of this layer was varied from 10^{13} to $5x10^{16}$ cm^{-3}. In line with previous studies, it was found that the open circuit voltage (V_{OC}) decreases as the defect density increases regardless of the dopant type (see Figure 4.19-a and Figure 4.19-b)[56]. Similarly, it was observed that as the doping concentration increases in the active layer, V_{oc} increases both for n-type and p-type DS PbS inks (see Figure 4.19-a and Figure 4.19-b). In accordance with the previous reports, this behavior was attributed to the reduction in the reverse saturation current with an increase in the dopant concentration, which have been known to have detrimental effects on the fill factor (FF) and PCE.[77]

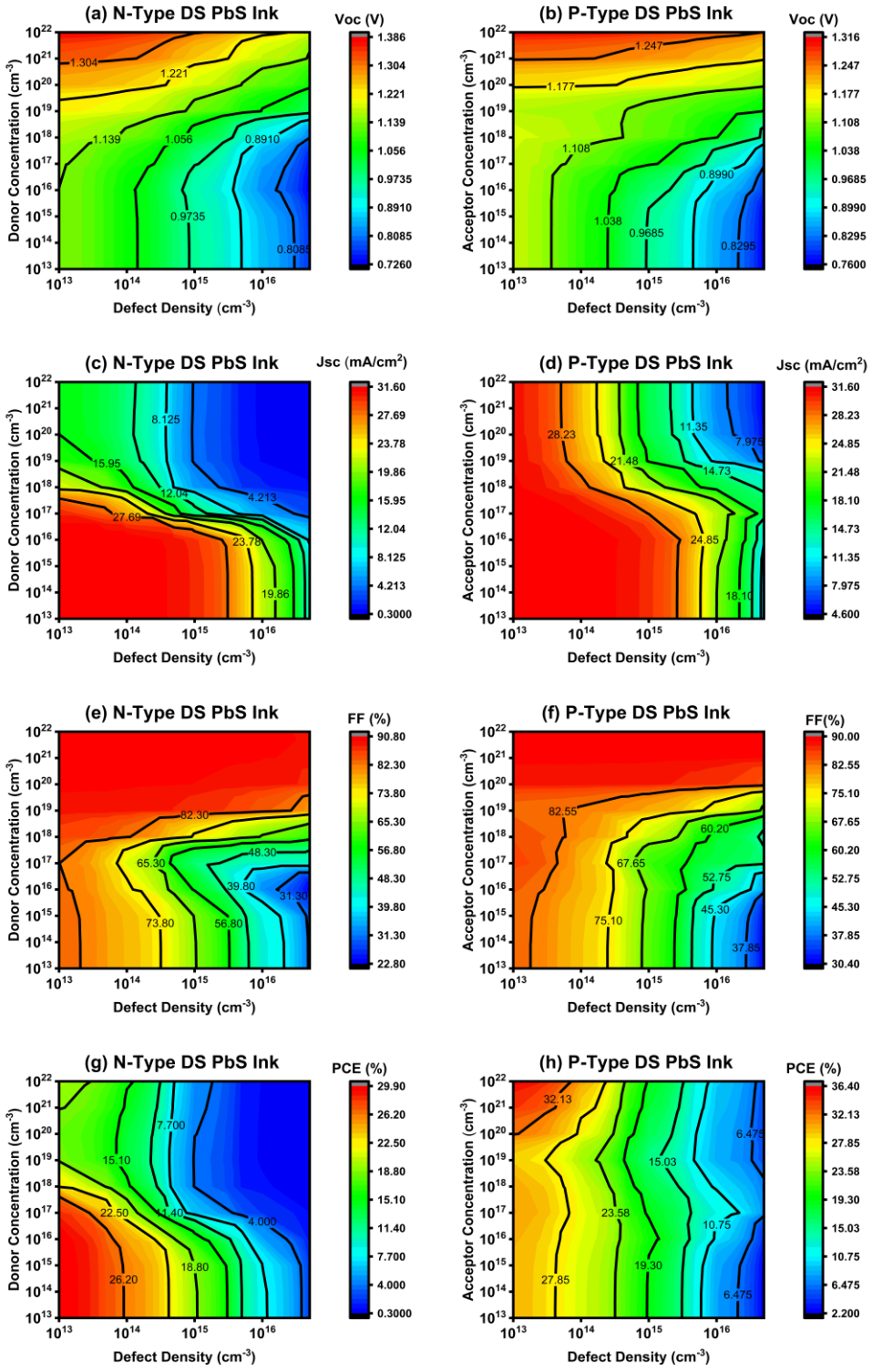

Figure 4.19. Concurrent effect of donor concentration and acceptor concentration vs. defect density on Voc (**a**,**b**), Jsc (**c**,**d**), FF (**e**,**f**), and PCE (**g**,**h**) parameters for the champion cell structure. The thickness of DS PbS ink was fixed at 300nm.

Interestingly, the effect of dopant concentration on J_{sc} shows a strong dependence on the defect concentration. At lower dopant concentrations, higher J_{sc} values were recorded for both dopant types. This was assigned to the wider depletion width which has been known to lead to a higher photogenerated carrier collection.[48] However, at higher dopant concentrations, the response of J_{sc} to the increase in defect concentration depends more on the dopant type. As represented in Figure 4.19-d, for the p-type, higher J_{sc} values can be attainable even at higher defect densities. Interestingly, at higher dopant concentrations, p-type ink was achieved to maintain high J_{sc} values which enhanced the PCE of cell. In addition, it was noted that FF follows a similar pattern as the V_{oc} for both n-type (Figure 4.19-e) and p-type device (Figure 4.19-f) since it is the product of V_{oc} and J_{sc}. Consequently, higher PCE values were achieved for the n-type ink at lower dopant concentrations (Figure 4.19-g) and for the p-type at higher dopant concentrations (Figure 4.19-h). Moreover, under the same conditions, the PCE was always higher for the p-type ink. This supports the observations of Choi et al for the p-type ink since they also reported a higher J_{sc} and consequently achieved higher PCE for the p-type ink when compared to their n-type counterparts.[75]

It was expected that the depletion width would decrease with increasing dopant concentration and thus the PCE would decrease with J_{SC}. However, unlike n-type inks, p-type inks unexpectedly showed higher performance at higher dopant concentrations. To further investigate the source of this unexpected result, the electrical field intensity within the device was simulated at a fixed defect density (10^{13} cm^{-3}). In accordance with previous reports, we found that higher acceptor concentration leads to a higher electric field and thus increases the carrier extraction rate.[78]

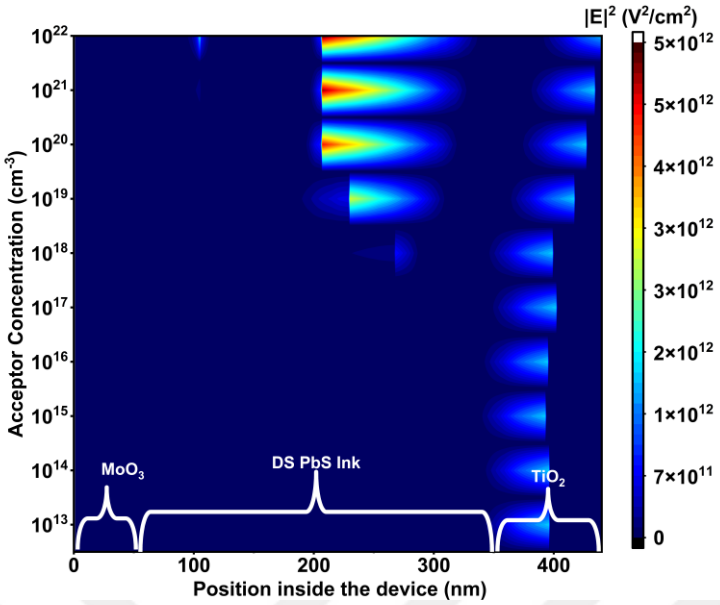

Figure 4.20. Electrical field intensity distribution in the ITO/TiO_2/ p-type DS PbS ink/ MoO_3/Au device architecture where the defect density was set at 10^{13} cm^{-3}.

The electrical field intensity ($|E|^2$) distribution was simulated within the device and the behavior is shown in Figure 4.20. It was observed that as the acceptor concentration increased, $|E|^2$ inside the active layer was increased towards TiO_2 ETL, which might lead to a more efficient carrier extraction.[79] Therefore, we conclude that, despite its small depletion width, the charge extraction rate of the device was enhanced due to increased $|E|^2$. Consequently, the high PCE that was achieved at the higher acceptor concentration values was attributed to the enhanced $|E|^2$ distribution within the device.

As a result, we found that the best performance is achievable for a p-type ink with a relatively high dopant concentration. Nevertheless, it is worth noting that p-type inks can achieve significantly higher performance parameters compared to their n-type counterparts, even when they have the same dopant concentration and defect densities. Furthermore, we noted that, at all dopant concentration values, n-type inks undergo rapid changes in the presence of increasing defect density, whereas p-type inks remain more stable. Therefore, according to our study, using inks with p-type

characteristics increases the device's defect tolerance and provides higher PCE at the same defect rates when compared to n-type inks.

4.6 Output of the Study

- Firdevs Aydın, Batuhan Uzun, Meysam Mirzaei-Saatlo, Elnaz Asghari, Demet Asil, “CdS/PbS Quantum Dot Solar Cells Based on Electrodeposited and in Situ Carbon Quantum Dot Doped CdS Thin Films as Electron Transport Layers”, 2024, ACS Applied Energy Materials (under review).
- Batuhan Uzun and Demet Asil, Unveiling the Potential of Direct Synthesized PbS CQD Ink Based Solar Cells Through Numerical Simulation, 2024, Scientific Reports (submitted).
- Batuhan Uzun, Firdevs Aydın and Demet Asil, Optimization of Direct-Synthesized PbS Ink for NIR Detectors, 2024, (under preparation).

CHAPTER 5

CONCLUSION AND FUTURE PROSPECT

The recently developed ink technologies (PTLE or DS), which is a candidate to eliminate the disadvantages of the conventional methods (SSLE) that has been used for many years, have both reduced the cost and played a major role in controlling surface defects to a certain point. Achieving the desired performance values (>10^{12} Jones specific detectivity) of these devices containing Nobel Prize-winning quantum dots depends primarily on investigating the source of possible losses and identifying the stages that cause them. In this thesis new approaches have been developed for the synthesis and ligand exchange of PbS CQDs, known to be key materials for future SWIR imagers, and these approaches have been implemented to the photodiode fabrication stages along with SCAPS simulation studies. Conventional SSLE method causes high dark current density in PbS CQD photodiodes and requires long process times. The main focus of this thesis was, therefore, comparing the PTLE method with theDS method in terms of device performance and device processing times.

Moreover, SCAPS simulation studies were conducted to determine the optimum performant PbS CQD Ink based SWIR photodiode device architecture. Two different scenarios were considered for SCAPS simulations. The first scenario involved light coming to the photodiode through ZnO (n-type) and was referred to as 'top illuminated'. The other scenario, referred to as 'bottom illuminated', featured light coming to the photodiode through PbS-EDT (p-type). In both cases, the device architecture was assumed to be ITO/ZnO/PbS Ink/PbS EDT/ITO. The top illuminated case had 7.30 mA.cm^{-2} current density whereas bottom illuminated case had 7.12 mA.cm^{-2} at -0.5V under 900nm light. The dark current density of the device is 2.15 x 10^{-7} mA.cm^{-2} at -0.5V. Apart from I-V results, top illumination exhibits ~40% at 980nm wavelength EQE whereas the bottom illumination's EQE is ~31%

at 980nm wavelength under AM 1.5 spectrum. Overall, the top illumination was considered as a better choice than bottom illumination.

As it is discussed, PTLE technique requires presynthesis of PbS CQDs that are synthesized via hot injection method where long-alkyl chain surfactant OA has to be exchanged for electirical conductivity. Thus, ligand exchange procedures must be applied to get PbS CQD ink form. Yet, the indispensable ligand exchange procedures cause problems such as high material cost, time consuming complex processes, difficulty in scalable production, and trap states in device. DS method, on the other hand, requires no complex ligand exchange mechanisms which makes the PbS CQD ink production process even simpler. In addition to that, the estimated PbS Ink production costs can be reduced from \$35.5 to 5 g^{-1} via DS method according to reported studies. However, there were some drawbacks for photodiodes that consist DS PbS Ink active layer such as slow rise/fall time and slightly lower EQE compared to photodiodes with PTLE PbS Ink. In this study, for instance, the photodiodes with DS PbS Ink showed ~ 32% EQE whereas PTLE PbS Ink device showed ~ 35% EQE at 980 nm wavelength. DS PbS Ink device, on the other hand, possess lower dark current density ~ 8 x 10^{-4} $mA.cm^{-2}$ where the PTLE PbS Ink device has ~ 4 x 10^{-3} $mA.cm^{-2}$. Because of this difference in dark current density, detectivity of DS PbS Ink device (~ 5 x 10^{11} Jones) is higher than PTLE PbS Ink device (~ 2 x 10^{11} Jones). Yet, PTLE PbS Ink device was able to respond to incident light faster than DS PbS Ink device since it has lower rise time and fall time. To be more specific, DS PbS Ink photodiode showed ~ 6 μs rise time and ~ 18 μs fall time while PTLE PbS Ink photodiode showed ~ 2 μs rise time and ~ 4 μs fall time. To overcome those problems, the DS method was slightly optimized by changing the place of butylamine which was called reaction 2 (R2) whereas conventional method was called reaction 1 (R1). In the R2 method, -SH groups were obtained prior to injection and the aim is to facilitate their combination with coordinated PbI_2 ions in DMF and formation of PbS QDs. Thus, the reaction time was shortened, preventing the clustering and growth of quantum dots due to the shortened time, thereby preventing the formation of large QDs that cause defects and disrupt the uniformity of size

distribution. The effect of it was observed in ITO/ZnO/DS PbS ink/PbS-EDT/Au device which was achieved $1.5x10^{13}$ Jones specific detectivity at 920 nm wavelength under -0.5 V bias. Moreover, the rise/fall time was also enhanced to 1.65 μs and 8.08 μs, respectively. In addition to this optimization, DS PbS ink was also studied in a SCAPS environment where different ETL and HTL combinations were simulated. The ITO/TiO_2(100nm)/DS PbS ink(300nm)/MoO_3(50nm)/Au architecture was found to be the best performant cell which achieved the PCE in the range of 20.24%. Following this study, the dopant type of DS PbS ink was investigated through this architecture. It was observed that p-type ink exhibits greater resilience to increasing defects and can achieve higher PCE (achieved max. 36.40%) compared to n-type ink (max. 29.90%). Even though the reported studies mainly focused on n-type ink, there is no reported study that implements the DS method to p-type ink. Therefore, the ability to synthesize p-type DS PbS ink should be of the utmost importance for future studies.

REFERENCES

1. Pejovic, V. *et al.* Infrared Colloidal Quantum Dot Image Sensors. *IEEE Trans Electron Devices* **69**, 2840–2850 (2022).

2. Jiang, J., Tsao, S., O'Sullivan, T., Razeghi, M. & Brown, G. J. Fabrication of indium bumps for hybrid infrared focal plane array applications. *Infrared Phys Technol* **45**, 143–151 (2004).

3. Efros, A. L. & Brus, L. E. Nanocrystal Quantum Dots: From Discovery to Modern Development. *ACS Nano* vol. 15 6192–6210 Preprint at https://doi.org/10.1021/acsnano.1c01399 (2021).

4. Kim, J. Y., Voznyy, O., Zhitomirsky, D. & Sargent, E. H. 25th anniversary article: Colloidal quantum dot materials and devices: A quarter-century of advances. *Advanced Materials* vol. 25 4986–5010 Preprint at https://doi.org/10.1002/adma.201301947 (2013).

5. Shrestha, A., Batmunkh, M., Tricoli, A., Qiao, S. Z. & Dai, S. Nahinfrarotaktive Bleichalkogenid-Quantenpunkte: Herstellung, postsynthetischer Ligandenaustausch und Anwendungen in Solarzellen. *Angewandte Chemie* **131**, 5256–5279 (2019).

6. Brus, L. E. A simple model for the ionization potential, electron affinity, and aqueous redox potentials of small semiconductor crystallites. *J Chem Phys* **79**, 5566–5571 (1983).

7. Harry, S. T. & Adekanmbi, M. A. Confinement Energy Of Quantum Dots And The Brus Equation. *International Journal Of Research -Granthaalayah* **8**, 318–323 (2020).

8. Talapin, D. V., Rogach, A. L., Haase, M. & Weller, H. Evolution of an ensemble of nanoparticles in a colloidal solution: Theoretical study. *Journal of Physical Chemistry B* **105**, 12278–12285 (2001).

9. Kagan, C. R. & Murray, C. B. Charge transport in strongly coupled quantum dot solids. *Nature Nanotechnology* vol. 10 1013–1026 Preprint at https://doi.org/10.1038/nnano.2015.247 (2015).

10. Murray, C. B., Kagan, C. R. & Bawendi, M. G. *Synthesis And Characterization Of Monodisperse Nanocrystals And Close-Packed Nanocrystal Assemblies*. Www.Annualreviews.Org (2000).

11. Lamer, V. K. & Dinegar, R. H. *Theory, Production and Mechanism of Formation of Monodispersed Hydrosols*.

12. Wagner, C. & Wagner, C. *Theorie Der Alterung von Niederschliigen Durch Umlosen (Ostwald-Reifung)*. vol. 65.

13. Lifshitz, I. M. & Slyozov, V. V. *The Kinetics Of Precipitation From Supersaturated Solid Solutions*. J. Phys. Chem. Solids Pergamon Press* vol. 19 (1961).

14. Talapin, D. V., Lee, J. S., Kovalenko, M. V. & Shevchenko, E. V. Prospects of colloidal nanocrystals for electronic and optoelectronic applications. *Chem Rev* **110**, 389–458 (2010).

15. Park, J., Joo, J., Soon, G. K., Jang, Y. & Hyeon, T. Synthesis of monodisperse spherical nanocrystals. *Angewandte Chemie - International Edition* vol. 46 4630–4660 Preprint at https://doi.org/10.1002/anie.200603148 (2007).

16. Hou, B. *et al.* Highly Monodispersed PbS Quantum Dots for Outstanding Cascaded-Junction Solar Cells. *ACS Energy Lett* **1**, 834–839 (2016).

17. Lee, J. W., Kim, D. Y., Baek, S., Yu, H. & So, F. Inorganic UV-Visible-SWIR Broadband Photodetector Based on Monodisperse PbS Nanocrystals. *Small* **12**, 1328–1333 (2016).

18. Liu, L. *et al.* Ligand and Solvent Effects on Hole Transport in Colloidal Quantum Dot Assemblies for Electronic Devices. *ACS Appl Nano Mater* **1**, 5217–5225 (2018).

19. Zheng, S., Chen, J., Johansson, E. M. J. & Zhang, X. iScience PbS Colloidal Quantum Dot Inks for Infrared Solar Cells. (2020) doi:10.1016/j.isci.

20. Wei, Y. *et al.* Stronger Coupling of Quantum Dots in Hole Transport Layer Through Intermediate Ligand Exchange to Enhance the Efficiency of PbS Quantum Dot Solar Cells. *Small Methods* (2024) doi:10.1002/smtd.202400015.

21. Zhang, X. *et al.* Probing and Controlling Surface Passivation of PbS Quantum Dot Solid for Improved Performance of Infrared Absorbing Solar Cells. *Chemistry of Materials* **31**, 4081–4091 (2019).

22. Li, F. *et al.* Matrix Manipulation of Directly-Synthesized PbS Quantum Dot Inks Enabled by Coordination Engineering. *Adv Funct Mater* **31**, (2021).

23. Wang, Y. *et al.* Room-temperature direct synthesis of semi-conductive PbS nanocrystal inks for optoelectronic applications. *Nat Commun* **10**, (2019).

24. Lu, K. *et al.* High-Efficiency PbS Quantum-Dot Solar Cells with Greatly Simplified Fabrication Processing via “Solvent-Curing”. *Advanced Materials* **30**, (2018).

25. Stavrinadis, A., Pradhan, S., Papagiorgis, P., Itskos, G. & Konstantatos, G. Suppressing Deep Traps in PbS Colloidal Quantum Dots via Facile Iodide Substitutional Doping for Solar Cells with Efficiency >10%. *ACS Energy Lett* **2**, 739–744 (2017).

26. Bi, Y. *et al.* Infrared Solution-Processed Quantum Dot Solar Cells Reaching External Quantum Efficiency of 80% at 1.35 μm and Jsc in Excess of 34 mA cm−2. *Advanced Materials* **30**, (2018).

27. Liu, Y. *et al.* Breaking the Size Limitation of Directly-Synthesized PbS Quantum Dot Inks Toward Efficient Short-wavelength Infrared Optoelectronic Applications. *Angewandte Chemie International Edition* (2023) doi:10.1002/anie.202300396.

28. Li, F. *et al.* Matrix Manipulation of Directly-Synthesized PbS Quantum Dot Inks Enabled by Coordination Engineering. *Adv Funct Mater* **31**, (2021).

29. Romiluyi, O., Eatmon, Y., Ni, R., Rand, B. P. & Clancy, P. The efficacy of Lewis affinity scale metrics to represent solvent interactions with reagent salts in all-inorganic metal halide perovskite solutions. *J Mater Chem A Mater* **9**, 13087–13099 (2021).

30. Ren, H., Chen, J. De, Li, Y. Q. & Tang, J. X. Recent Progress in Organic Photodetectors and their Applications. *Advanced Science* vol. 8 Preprint at https://doi.org/10.1002/advs.202002418 (2021).

31. Bielecki, Z. *et al.* Review of photodetectors characterization methods. *Bulletin of the Polish Academy of Sciences: Technical Sciences* vol. 70 Preprint at https://doi.org/10.24425/bpasts.2022.140534 (2022).

32. Lee, J. U., Gipp, P. P. & Heller, C. M. Carbon nanotube p-n junction diodes. *Appl Phys Lett* **85**, 145–147 (2004).

33. Electronics Inc, W. *AN-LD17: Photodiode Basics: Selection & Operation*. www.teamWavelength.com (2020).

34. Saran, R. & Curry, R. J. Lead sulphide nanocrystal photodetector technologies. *Nature Photonics* vol. 10 81–92 Preprint at https://doi.org/10.1038/nphoton.2015.280 (2016).

35. Xu, Q. *et al.* Ultrafast Colloidal Quantum Dot Infrared Photodiode. *ACS Photonics* **7**, 1297–1303 (2020).

36. Ghosh, A. & Upadhyaya, A. S. Broad band antireflection coating on zinc sulphide simultaneously effective in SWIR, MWIR and LWIR regions. *Infrared Phys Technol* **52**, 109–112 (2009).

37. Choubey, B., Carlos, L. & Gouveia, P. *On Evolution of CMOS Image Sensors Supercamera-a Co-Axial Visible MIR and THz Focal Plane Array View Project On Evolution of CMOS Image Sensors*. https://www.researchgate.net/publication/274380537 (2014).

38. Heves, E. & Gurbuz, Y. PbS colloidal quantum dot photodiodes for SWIR detection. in *Procedia Engineering* vol. 47 1426–1429 (Elsevier Ltd, 2012).

39. Jung, B. K. *et al.* Suppressing the Dark Current in Quantum Dot Infrared Photodetectors by Controlling Carrier Statistics. *Adv Opt Mater* **10**, (2022).

40. Liu, J. *et al.* A near-infrared colloidal quantum dot imager with monolithically integrated readout circuitry. *Nat Electron* **5**, 443–451 (2022).

41. Dong, C. *et al.* Long-Wavelength Lead Sulfide Quantum Dots Sensing up to 2600 nm for Short-Wavelength Infrared Photodetectors. *ACS Appl Mater Interfaces* **11**, 44451–44457 (2019).

42. Xiao, X. *et al.* High quality silicon: Colloidal quantum dot heterojunction based infrared photodetector. *Appl Phys Lett* **116**, (2020).

43. Wang, J. & Chen, J. High-sensitivity silicon: PbS quantum dot heterojunction near-infrared photodetector. *Surfaces and Interfaces* **30**, (2022).

44. Masala, S. *et al.* The Silicon:Colloidal Quantum Dot Heterojunction. *Advanced Materials* **27**, 7445–7450 (2015).

45. García De Arquer, F. P., Armin, A., Meredith, P. & Sargent, E. H. Solution-processed semiconductors for next-generation photodetectors. *Nature Reviews Materials* vol. 2 Preprint at https://doi.org/10.1038/natrevmats.2016.100 (2017).

46. Gilmore, R. H. *et al.* Epitaxial Dimers and Auger-Assisted Detrapping in PbS Quantum Dot Solids. *Matter* **1**, 250–265 (2019).

47. Burgelman, M., Nollet, P. & Degrave, S. *Modelling Polycrystalline Semiconductor Solar Cells*. www.elsevier.com/locate/tsf.

48. Kumar, S., Bharti, P. & Pradhan, B. Performance optimization of efficient PbS quantum dots solar cells through numerical simulation. *Sci Rep* **13**, (2023).

49. Liu, Y. *et al.* Merging Passivation in Synthesis Enabling the Lowest Open-Circuit Voltage Loss for PbS Quantum Dot Solar Cells. *Advanced Materials* **35**, (2023).

50. Wang, D. *et al.* How to minimize voltage and fill factor losses to achieve over 20% efficiency lead chalcogenide quantum dot solar cells: Strategies expected through numerical simulation. *Appl Energy* **341**, (2023).

51. Qin, I., Shah, A., Xu, H., Chylak, B. & Wong, N. *Advances in Wire Bonding Technology for Different Bonding Wire Material*. http://meridian.allenpress.com/ism/article-pdf/2015/1/000406/2256525/isom-2015-wp33.pdf (2015).

52. Zhang, X. *et al.* Inorganic CsPbI3 Perovskite Coating on PbS Quantum Dot for Highly Efficient and Stable Infrared Light Converting Solar Cells. *Adv Energy Mater* **8**, (2018).

53. Bederak, D. *et al.* Comparing Halide Ligands in PbS Colloidal Quantum Dots for Field-Effect Transistors and Solar Cells. *ACS Appl Nano Mater* **1**, 6882–6889 (2018).

54. Jeong, K. S. *et al.* Enhanced mobility-lifetime products in PbS colloidal quantum dot photovoltaics. *ACS Nano* **6**, 89–99 (2012).

55. Williams, A. E. *et al.* Perovskite processing for photovoltaics: A spectro-thermal evaluation. *J Mater Chem A Mater* **2**, 19338–19346 (2014).

56. Hossain, M. K. *et al.* Effect of Various Electron and Hole Transport Layers on the Performance of CsPbI3-Based Perovskite Solar Cells: A Numerical Investigation in DFT, SCAPS-1D, and wxAMPS Frameworks. *ACS Omega* **7**, 43210–43230 (2022).

57. Touafek, N., Mahamdi, R. & Dridi, C. *Boosting the Performance of Planar Inverted Perovskite Solar Cells Employing Graphene Oxide as HTL*. *Digest Journal of Nanomaterials and Biostructures* vol. 16.

58. Dahal, B., Rezaee, M. D., Gotame, R. C. & Li, W. Exploring the performance of perovskite solar cells with dual hole transport layers via SCAPS-1D simulation. *Mater Today Commun* **36**, (2023).

59. Sawicka-Chudy, P. *et al.* Simulation of TiO2/CuO solar cells with SCAPS-1D software. *Mater Res Express* **6**, (2019).

60. Raoui, Y. *et al.* Performance analysis of MAPbI3 based perovskite solar cells employing diverse charge selective contacts: Simulation study. *Solar Energy* **193**, 948–955 (2019).

61. Gan, Y. *et al.* Numerical investigation energy conversion performance of tin-based perovskite solar cells using cell capacitance simulator. *Energies (Basel)* **13**, (2020).

62. Yousuf, M. H., Saeed, F. & Tauqeer, H. A. Numerical Investigation of Cu 2 O as Hole transport layer for High-Efficiency CIGS solar cell. (2021) doi:10.20944/preprints202110.0326.v1.

63. Sahoo, A. & Mangal, S. Performance analysis of tin-based perovskite solar cell with MoO3 as a HTL under a wide temperature range. *Mater Today Proc* (2023) doi:10.1016/j.matpr.2023.06.109.

64. Chabri, I., Oubelkacem, A. & Benhouria, Y. Numerical development of lead-free Cs2TiI6-based perovskite solar cell via SCAPS-1D; Numerical

development of lead-free Cs2TiI6-based perovskite solar cell via SCAPS-1D. doi:10.1051/e3sconf/202233600050ï.

65. Rahman, M. B., Noor-E-Ashrafi, N., Miah, M. H., Khandaker, M. U. & Islam, M. A. Selection of a compatible electron transport layer and hole transport layer for the mixed perovskite FA0.85Cs0.15Pb (I0.85Br0.15)3, towards achieving novel structure and high-efficiency perovskite solar cells: a detailed numerical study by SCAPS-1D. *RSC Adv* **13**, 17130–17142 (2023).

66. Moulaoui, L., Bajjou, O., Najim, A., Archi, M. & Rahmani, K. Numerical simulation of the NiO as hole transport layer in CH3NH3PbBr3perovskite based-solar cell using SCAPS-1D. in *2022 2nd International Conference on Innovative Research in Applied Science, Engineering and Technology, IRASET 2022* (Institute of Electrical and Electronics Engineers Inc., 2022). doi:10.1109/IRASET52964.2022.9737984.

67. Islam, M. S. *et al.* Defect study and modelling of SnX3-based perovskite solar cells with SCAPS-1D. *Nanomaterials* **11**, (2021).

68. Putra, N. M. D., Sugianto, Marwoto, P., Murtafiatin, R. & Permadis, D. P. The SCAPS-1D modeling of ZnO/CdS/CdTe thin film: Analysis of thickness and stoichiometric fraction of absorber layer on solar cell performance. in *Journal of Physics: Conference Series* vol. 1918 (IOP Publishing Ltd, 2021).

69. Ait-Wahmane, Y. *et al.* Comparison study between ZnO and TiO2in CuO based solar cell using SCAPS-1D. in *Materials Today: Proceedings* vol. 52 166–171 (Elsevier Ltd, 2021).

70. Memari, A., Javadian Sarraf, M., Seyyed Mahdavi Chabok, S. J. & Motevalizadeh, L. Comprehensive guidance for optimizing the colloidal quantum dot (CQD) Perovskite solar cells: experiment and simulation. *Sci Rep* **13**, (2023).

71. Mohandes, A., Moradi, M. & Kanani, M. Numerical analysis of high performance perovskite solar cells with stacked ETLs/C60 using SCAPS-1D device simulator. *Opt Quantum Electron* **55**, (2023).

72. Oyedele, S. O. & Aka, B. Numerical Simulation of Varied Buffer Layer of Solar Cells Based on Cigs. *Modeling and Numerical Simulation of Material Science* **07**, 33–45 (2017).

73. Song, J. H., Mai, X. D., Jeong, S. & Kim, Y. H. Hysteresis and Photoinstability Caused by Mobile Ions in Colloidal Quantum Dot Photovoltaics. *Journal of Physical Chemistry Letters* **8**, 5259–5263 (2017).

74. Diekmann, J. *et al.* Pathways toward 30% Efficient Single-Junction Perovskite Solar Cells and the Role of Mobile Ions. *Solar RRL* **5**, (2021).

75. Choi, M. J. *et al.* Cascade surface modification of colloidal quantum dot inks enables efficient bulk homojunction photovoltaics. *Nat Commun* **11**, (2020).

76. Khalaf, G. M. G. *et al.* PbS Colloidal Quantum Dots Infrared Solar Cells: Defect Information and Passivation Strategies. *Small Science* vol. 3 Preprint at https://doi.org/10.1002/smsc.202300062 (2023).

77. Sunny, A., Rahman, S., Khatun, M. M. & Ahmed, S. R. Al. Numerical study of high performance HTL-free CH3NH3SnI3-based perovskite solar cell by SCAPS-1D. *AIP Adv* **11**, (2021).

78. . F. S. Effect Of The Electric Field On The Different Electrical Parameters Of A Solar Cell. *Int J Res Eng Technol* **07**, 16–21 (2018).

79. Banik, S., Das, A., Das, B. K. & Islam, N. Numerical simulation and performance optimization of a lead-free inorganic perovskite solar cell using SCAPS-1D. *Heliyon* **10**, (2024).